

**OPEN ACCESS**

# Editors' Choice—Visualizing the Impact of the Composite Cathode Microstructure and Porosity on Solid-State Battery Performance

To cite this article: Philip Minnmann *et al* 2024 *J. Electrochem. Soc.* **171** 060514






View the [article online](#) for updates and enhancements.

## You may also like

- [Understanding the battery safety improvement enabled by a quasi-solid-state battery design](#)  
Luyu Gan, , Rusong Chen et al.
- [Recycling of solid-state batteries—challenge and opportunity for a circular economy?](#)  
Martine Jacob, Kerstin Wissel and Oliver Clemens
- [Observation of Dirac-like surface state bands on the top surface of BiSe](#)  
H. Lohani, K. Majhi, R. Ganesan et al.



## Editors' Choice—Visualizing the Impact of the Composite Cathode Microstructure and Porosity on Solid-State Battery Performance

Philip Minnmann,<sup>1,2,z</sup>  Johannes Schubert,<sup>1,2,z</sup>  Sascha Kremer,<sup>1,2</sup>  René Rekers,<sup>1,2</sup>  
Simon Burkhardt,<sup>1,2</sup> Raffael Ruess,<sup>1,2</sup> Anja Bielefeld,<sup>1,2</sup>  Felix H. Richter,<sup>1</sup> and  
Jürgen Janek<sup>1,2,3,z</sup> 

<sup>1</sup>Institute for Physical Chemistry, Justus-Liebig-University Giessen, Germany

<sup>2</sup>Center for Materials Research, Justus-Liebig-University Giessen, Germany

<sup>3</sup>BELLA, Institute for Nanotechnology, Karlsruhe Institute of Technology, Karlsruhe, Germany

The kinetics of composite cathodes for solid-state batteries (SSBs) relies heavily on their microstructure. Spatial distribution of the different phases, porosity, interface areas, and tortuosity factors are important descriptors that need accurate quantification for models to predict the electrochemistry and mechanics of SSBs. In this study, high-resolution focused ion beam-scanning electron microscopy tomography was used to investigate the microstructure of cathodes composed of a nickel-rich cathode active material (NCM) and a thiophosphate-based inorganic solid electrolyte (ISE). The influence of the ISE particle size on the microstructure of the cathode was visualized by 3D reconstruction and charge transport simulation. By comparison of experimentally determined and simulated conductivities of composite cathodes with different ISE particle sizes, the electrode charge transport kinetics is evaluated. Porosity is shown to have a major influence on the cell kinetics and the evaluation of the active mass of electrochemically active particles reveals a higher fraction of connected NCM particles in electrode composites utilizing smaller ISE particles. The results highlight the importance of homogeneous and optimized microstructures for high performance SSBs, securing fast ion and electron transport.

© 2024 The Author(s). Published on behalf of The Electrochemical Society by IOP Publishing Limited. This is an open access article distributed under the terms of the Creative Commons Attribution 4.0 License (CC BY, <http://creativecommons.org/licenses/by/4.0/>), which permits unrestricted reuse of the work in any medium, provided the original work is properly cited. [DOI: 10.1149/1945-7111/ad510e]



Manuscript submitted March 24, 2024; revised manuscript received May 13, 2024. Published June 11, 2024.

Supplementary material for this article is available [online](#)

Since their commercialization more than 30 years ago, lithium-ion batteries (LIBs) have greatly influenced everyday life from enabling handheld electronic devices that can operate for days to the first electrified vehicles able to drive hundreds of kilometers on a single charge. However, this type of battery, even though still making progress, is slowly approaching fundamental physicochemical limitations in terms of energy density and power density.<sup>1</sup> For a further increase, new concepts are necessary. Among the most promising concepts are solid-state batteries (SSBs), which replace flammable organic electrolytes used in LIBs with a solid electrolyte.<sup>2</sup> To date, numerous classes of inorganic solid electrolytes (ISEs) have been explored and thiophosphate-based ISEs appear particularly promising due to their exceptionally high ionic conductivity exceeding 20 mS cm<sup>-1</sup> and favorable mechanical properties, that allow room temperature operation and processing, respectively.<sup>3–6</sup> However, there are still challenges that limit the SSB performance and consequently their practical application.<sup>7</sup>

While on the anode side, mostly two-dimensional interfaces between the ISE and high-capacity anodes such as lithium metal or silicon are investigated,<sup>8–10</sup> three-dimensional composites are used as the cathode.<sup>11–13</sup> These composites consist of the cathode active material (CAM), the ISE, functional additives (such as polymer binders or carbons) and a (hardly avoidable) residual porosity. The arrangement of the individual constituents is denoted as microstructure of the cathode composite and is of paramount importance for the SSB performance.<sup>14–16</sup> In an ideal cathode, the porosity is minimized, the CAM content is maximized (it is the only constituent storing charge), and the ISE is distributed homogeneously forming low resistance charge transport pathways.<sup>12,13,17</sup> This means that the cathode microstructure must conduct ions and electrons and provide a large interfacial contact area between ISE and CAM to ensure rapid transfer of lithium during charging and discharging.<sup>12</sup> However, charge transport pathways are often tortuous and charge carriers must travel longer distances than one might initially assume

based on the geometric dimensions. This can be quantified by “tortuosity factors,” which correlate effective transport properties and bulk properties of the respective phases in a composite microstructure, and which have become an important metric in microstructural optimization<sup>14,18</sup> even though their proper determination and meaningfulness is still under debate.<sup>19,20</sup>

In LIBs, cathodes are manufactured as porous components, that can be infiltrated by liquid electrolyte, thus enabling sufficient wetting of the CAM in all cathode regions as well as short charge transport pathways.<sup>21,22</sup> In SSBs, however, the picture is different as the ISE is already a constituent of the cathode during the manufacturing process. Therefore, uniform distribution and intimate contact between CAM and ISE particles must be achieved during cell fabrication. Consequently, the microstructure of these cathodes is more complex than in LIBs. In this context, thiophosphate-based ISEs have unique mechanical properties that distinguishes them from other material classes. In particular, their malleability allows densification at low temperature without requiring energy intensive sintering.<sup>23</sup>

Several research groups have studied the cathode microstructure by modelling or electrical transport measurements.<sup>14,15,18,24–36</sup> Key findings include that cell microstructure and resulting properties depend on the employed materials, composition,<sup>14,15,18,25,28,29,35</sup> particle sizes<sup>16,33,34,36–39</sup> and manufacturing conditions.<sup>40–43</sup> For instance, Shi et al.<sup>34</sup> introduced the ratio of ISE to CAM as a determining metric and Cronau et al. expanded this concept to a detailed experimental study on the achievable capacity in SSBs.<sup>44</sup>

Additional to model-based approaches and electrochemical measurements, three-dimensional tomography and microstructural reconstruction are important to visualize and understand the real microstructure. Methods that allow such reconstructions are e.g. X-ray computed tomography (CT) and focused ion beam scanning electron microscopy (FIB-SEM). First studies have already reported such microstructures<sup>45–50</sup> and delivered valuable input for modelling groups that can use these reconstructions to simulate charge transport and battery operation on real models. For instance, chemo-mechanical failure of composite cathodes was investigated<sup>51,52</sup> and globally obtained data such as the charge transfer resistance of a cathode were

<sup>z</sup>E-mail: [philip.minnmann@phys.chemie.uni-giessen.de](mailto:philip.minnmann@phys.chemie.uni-giessen.de); [johannes.schubert@phys.chemie.uni-giessen.de](mailto:johannes.schubert@phys.chemie.uni-giessen.de); [juergen.janek@phys.chemie.uni-giessen.de](mailto:juergen.janek@phys.chemie.uni-giessen.de)

correlated to the microscopic processes, i.e. areal resistance of the ISE-CAM interface.<sup>47</sup>

So far, there are few studies correlating actual charge transport measurements of thiophosphate-based SSB cathodes<sup>35,50,53</sup> with the microstructural information obtained from tomography. These investigate mostly only small volumes (in the range of a few thousands of  $\mu\text{m}^3$ ) or larger volumes with lower resolution (> 300 nm). Nevertheless, these studies provide valuable insight into the fundamental microstructural features that limit SSB cathode performance. Hlushkou et al. investigated the influence of pores on the charge transport in  $\text{LiCoO}_2$ -based electrodes and found that porosity has a significant effect on the ionic charge transport in such structures.<sup>53</sup> The same group reported detailed reconstructions and investigated the microstructure of  $\text{LiNi}_x\text{Co}_y\text{Mn}_z\text{O}_2$ -based composite cathodes using ISEs ( $\beta\text{-Li}_3\text{PS}_4$  and  $\text{Li}_6\text{PS}_5\text{Br}$ ) with different particle morphologies.<sup>47</sup> Iwamoto et al. used nano-CT to obtain cathode reconstructions and simulated charge transport parameters for three different ISE particle sizes (75 $\text{Li}_2\text{S}$ -25 $\text{P}_2\text{S}_5$  glass).<sup>48</sup> They found that clustering of active material particles, which is one of the mechanisms that limits SSB performance, can be reduced by smaller ISE particles. However, due to the nature of the employed technique, they could not determine and consider porosity in their reconstructions.

A detailed study visualizing the influence of thiophosphate-based ISE particle size on the microstructure of composite cathodes and investigating the effects on charge transport is reported here for the first time, to the best of our knowledge. We compare experimental and simulated charge transport in composite cathodes composed of agglomerated single crystals of  $\text{LiNi}_{0.83}\text{Co}_{0.11}\text{Mn}_{0.06}\text{O}_2$  (NCM) and the thiophosphate-based glassy ISE  $\text{Li}_3\text{PS}_4$ -0.5 $\text{LiI}$  with different particle sizes. We correlate the results to the microstructure obtained by highly resolved FIB-SEM tomography on large (several  $10^5 \mu\text{m}^3$ ) cathode volumes. A complementary investigation of the electrochemical performance, the utilization levels of CAM and the chemomechanics of these cathodes provides important information for modelling groups and are used to develop guidelines for the further optimization of the composite cathode.

## Experimental

All solids used in this study were dried at 200 °C under dynamic vacuum for 12 h using a vacuum drying oven (Büchi, Switzerland). Unless stated otherwise, all experiments were performed under inert gas atmosphere; either in an Ar filled glovebox (LabMaster, MBraun, Germany) with  $\text{H}_2\text{O}$  and  $\text{O}_2$  concentration below 0.1 ppm and  $\text{N}_2$  concentration below 1 ppm, or by using sealed containers for components and materials filled with dry Ar atmosphere.

**Synthesis.**—Glassy  $\text{Li}_3\text{PS}_4$ -0.5 $\text{LiI}$  (ISE) was synthesized via a mechanochemical route using stoichiometric amounts of  $\text{P}_2\text{S}_5$  (Sigma Aldrich),  $\text{LiI}$  (Sigma Aldrich) and  $\text{Li}_2\text{S}$  (Sigma Aldrich) (2 g in total). Precursors were mixed in a planetary ball mill (Pulverisette 7, Fritsch, Germany) for 12 h with a rotational speed of 450 rpm using a 70 ml zirconia jar and 20 pieces of zirconia milling media of 10 mm diameter. Three batches of ISE powder were synthesized in this way. In order to obtain ISE powders with smaller particle sizes, additional milling steps were conducted for two of the batches. For this, the two batches were ground further for 4 h at 450 rpm using zirconia milling media of 3 mm diameter and 1 mm diameter, respectively, with a milling media-to-powder weight ratio of 30:1. To reduce the amount of powder adhering to the milling media, and hence, increasing the yield, five drops of anhydrous heptane were added into the jar prior to grinding. Mixing as well as grinding were suspended after every 15 min for 15 min to prevent overheating of the sample. After removal of the sample from the jar, all products were ground in an agate mortar for 5 min by hand to crush agglomerates of ISE. The ISE powders obtained from grinding with milling media of 10 mm, 3 mm and 1 mm diameter and

composites prepared from these are referred to as BM10, BM03 and BM01 (BM corresponds to “ball milled”), respectively, in the following.

**Cell fabrication and testing.**—For SSB cell fabrication, an in house developed housing was used.<sup>54</sup> Initially, 60 mg of  $\text{Li}_6\text{PS}_5\text{Cl}$  (LPSCI) (NEI Corporation, Somerset, USA) were put into a 10 mm diameter polyetheretherketone (PEEK) cylinder and compacted by a hand press using stainless steel pistons. Cathode composites were prepared for each batch of ISE with differing particle sizes of the ISE powder. For this, agglomerated single-crystals of  $\text{LiNi}_{0.83}\text{Mn}_{0.06}\text{Co}_{0.11}\text{O}_2$  ( $D_{50} = 3\text{--}5 \mu\text{m}$ , MSE Supplies, USA) and  $\text{Li}_3\text{PS}_4$ -0.5 $\text{LiI}$  in the weight ratio of 70:30 were thoroughly mixed for 15 min by hand in an agate mortar. 12 mg of composite material (equivalent to a CAM loading of  $10.7 \text{ mg cm}^{-2}$ ) was homogeneously distributed on the LPSCI separator layer, and the resulting pellet was densified at room temperature by uniaxial pressure of approx. 380 MPa for 3 min. Finally, an indium foil disc (9 mm diameter, 100  $\mu\text{m}$ , ChemPur, Germany) and a lithium foil disc (6 mm diameter, 100  $\mu\text{m}$ , China Energy Lithium, PRC) were placed on the separator layer leading to an  $\text{In}/(\text{InLi})_x$  two-phase mixture that served as anode with a stable potential of 0.62 V vs  $\text{Li}^+/\text{Li}$ .<sup>55</sup>

All resulting SSB cells were cycled in a Maccor battery cyler at 25 °C with an applied stack pressure of 30 MPa. Galvanostatic charging and discharging was conducted between 2 V and 3.7 V with C-rates of 0.1 C, 0.2 C, 0.5 C, 1 C and 2 C (1 C = 200  $\text{mA g}^{-1}$ ) increasing every three cycles.

**Conductivity measurements.**—For measurements of the ionic conductivity of the synthesized ISEs an ion-blocking symmetric cell configuration was used in which the ISE was confined on both sides with steel pistons. For this, approx. 100 mg of ISE were filled in the PEEK cylinder and subsequently pressed at room temperature with uniaxial pressure of approx. 380 MPa.

For conductivity measurements of the cathode two types of symmetric cell configurations containing 50 mg or 100 mg of the composite cathode material were prepared. Please note that no conductive additive was added to avoid additional decomposition reactions.

For measurements of the electronic conductivity the composite was put into the PEEK cylinder, confined on both sides with steel pistons and subsequently compacted at 380 MPa for 3 min. For measurement of the ionic conductivity a LPSCI separator layer with a thickness of approx. 400  $\mu\text{m}$  was formed by compaction of the powder at 380 MPa for 3 min. 25 mg or 50 mg of the composite cathode material were then distributed on both sides followed by a final densification step.

Electrochemical impedance spectroscopy was carried out with a VMP-300 potentiostat (Biologic, France) at ambient temperature. Cells were mounted in a steel frame which allowed to maintain a pressure of about 100 MPa throughout the measurement. Potentiostatic electrochemical impedance spectra (PEIS) of symmetric cells were recorded at open circuit voltage (OCV) in the frequency range of 3 MHz to 10 mHz with an amplitude of 10 mV.

**Particle size analysis.**—The particle size of the ISE was determined by laser scattering. A small amount of the respective sample was dispersed in a solution of polyisobutylene and anhydrous xylene. The dispersion was subsequently ultrasonicated for 15 min. Measurements were performed outside of a glovebox in a HELOS particle size analyzer (SympaTec GmbH, Germany). Due to a short timeframe of the measurement and the dispersion in xylene, we assume no significant change in the particle size and morphology.

**FIB-SEM.**—Plasma-FIB-SEM (PFIB-SEM) tomography of three composite pellets (differing ISE particle size and without carbon) was carried out on a XEIA3 (Tescan, Czech Republic) using an Xe-plasma ion source. Pellets were coated with a thin platinum layer by sputter deposition and subsequently the region of interest

was coated with 10–15  $\mu\text{m}$  of platinum using the gas injection system of the instrument. A U-shaped trench was milled into the surface allowing for imaging of the cross-sectional area. To attenuate curtaining, a polishing step was carried out prior to tomography. Sectioning was performed automatically using the 3D acquisition wizard of the software with a current of 36 nA and with a slice distance of 100 nm. Secondary electron (SE) and back scattered electron (BSE) SEM images were recorded with a resolution of 100 nm, which results in cubic voxel dimensions. All sample transfers were conducted under vacuum or inert Ar-atmosphere using a VCT transfer module (LEICA, Germany).

**Image processing and segmentation.**—Processing of the images acquired by the BSE and the SE detectors was implemented with *Fiji ImageJ* and *Python 3.7*. First, in order to align all images of the image stacks properly, slight drifting of the imaged cross-section area throughout the measurement was corrected using the *MultiStackReg* plugin of *ImageJ*, enabling identical drift correction of BSE and SE image stacks. Potential inhomogeneous illuminations of images were reduced by division of the image with a strongly blurred version of itself. Finally, curtaining effects visible only in SE images were attenuated with the *Stripes Filter* function of the *Xlib* plugin and the image contrast was normalized.

As an attempt to improve segmentation of pores as well as interfaces, a segmentation method based on machine learning techniques was implemented. The employed machine learning model consists of the first two convolutional layers of a pre-trained *VGG16 CNN* model used for feature extraction and a random forest classifier used for the pixelwise classification task.<sup>56</sup> Details are described in Sect. S3. The implementation in *Python* was performed using *Keras* and *Scikit-learn*.<sup>57,58</sup> The segmented image was generated by combination of the segmentation of BSE and SE images. Several impurities of an unknown material (possibly fragments of a mortar) were observed in the BM01 sample. Since the volume fraction was small and fragments could be reliably identified by eye, the phase was segmented manually on the respective slices.

**Microstructure analysis.**—The three-dimensional reconstruction obtained from the segmented images and all subsequent methods for its microstructural analysis and characterization were implemented in *Python*. The volume fractions of CAM, ISE and pores were directly calculated from the reconstructed volume by counting all voxels belonging to the respective phase. Surface areas for each phase and respective interface areas were calculated using the marching cubes algorithm by *Scikit-learn*. With the surface areas  $S$  of each phase, the interface area  $S_{a-b}$  between phases in a system containing three phases (a, b, c) was then calculated with Eq. 1.<sup>59</sup>

$$S_{a-b} = \frac{1}{2}(S_a + S_b - S_c) \quad [1]$$

Chord length distributions CLD of CAM and ISE phase were determined using the *Python* package *PoreSpy*.<sup>60</sup> Chords are linear segments lying inside the phase of interest and with both ends trimmed at the phase boundary.<sup>61</sup> Hence, the CLD may allow to draw conclusions on the morphology of the respective phase and with regard to the investigated composite, in particular, potential clustering of phases. Chords were applied along each axis of the volume with a distance of two voxels between adjacent chords. Chords intersecting the volume of interest boundaries were discarded as they are artificially truncated, and thus, would distort the distribution.

**Determination of the tortuosity.**—To further assess the influence of morphology on the transport properties, tortuosities of CAM and ISE phases were determined by random walk simulations using *Pytrax* and by a flux-based method using *GeoDict*.<sup>62,63</sup> For random walk simulations, initially, a total of 2000 walkers were randomly

distributed in either the CAM phase or the ISE phase. Every timestep, the walkers were allowed to move in orthogonal directions to adjacent voxels and the respective mean square displacement (*MSD*) was recorded periodically. In order to prevent artificial confinement of the walker and introduction of an upper limit of the *MSD*, the reconstructed volume was extended on each side by mirroring, which allows the walker to leave the volume. Afterwards, the *MSD* was plotted as a function of time steps, resulting in a roughly linear curve, and the tortuosity was determined from the inverse slope considering that the slope of the respective curve is unity in free space. To ensure a sufficient number of time steps, simulations were performed multiple times with an increasing number of time steps for each simulation. For the flux-based method, *GeoDict's ConductoDict* module was used to determine the partial conductivities from which the tortuosities were subsequently calculated.

## Results

**Solid electrolyte particle size influences effective conductivity.**—We prepared glassy  $\text{Li}_3\text{PS}_4\text{-}0.5\text{LiI}$  solid electrolyte with three different particle sizes (BM10, BM03, BM01) using solvent-assisted ball milling with three different milling media sizes. Figures 1a–1c compare the SEM images of these samples. We note that all three samples exhibit a similar particle morphology, which indicates that no severe damage was inflicted to the particles by ball milling. In a first qualitative assessment, it can be observed that the number of larger particles is reduced by the ball milling steps with 3 mm or 1 mm milling media, which results in a much larger number of smaller particles.

Using these SEM images, the particle size can be quantified, as shown in Figs. 1a–1c. Evidently, the particle size decreases when smaller milling media are employed, i.e. in the BM10 sample, several large particles with diameter  $d > 20 \mu\text{m}$  can be observed, while in the BM03 sample only few larger particles are found. In contrast, the BM01 sample does not show particles with  $d > 20 \mu\text{m}$ , however, the general particle size is slightly larger than the one in the BM03 sample. This is also evident in the particle size distribution (PSD) data obtained by laser diffraction. The  $d_{50}$  values decrease from  $d_{50} = 7.41 \mu\text{m}$  for BM10 to  $d_{50} = 4.93 \mu\text{m}$  for the BM03 sample. While with  $d_{50} = 5.93 \mu\text{m}$  the BM01 sample also shows a decrease in particle size compared to the BM10 sample, the BM03 sample apparently exhibits overall the smallest particle sizes. Based on the SEM images (Fig. 1c), we attribute this observation to particle re-agglomeration in the suspension, which could not be avoided entirely and can be responsible for the additional change of slope around  $10 \mu\text{m}$  in the PSD of the BM01 sample. Interestingly, the distribution of particle sizes becomes narrower for the BM03 and BM01 sample. A narrow PSD can result in more homogeneous microstructures of cathodes which may improve their charge transport properties.

The effective reduction of the particle sizes by use of smaller milling media can be explained by the increase of the collision frequency between the sample and the milling media. Smaller milling media are, at a given total mass, more numerous than larger milling media and can create more collisions per time unit than their larger counterparts. For a further reduction of the particle size, we assume that particle re-agglomeration must be avoided, for instance by use of dispersing agents and surfactants.

We determined the room temperature ionic conductivity to be  $\sigma_{\text{ion}} = 2.0 \text{ mS cm}^{-1}$  for BM10,  $\sigma_{\text{ion}} = 1.7 \text{ mS cm}^{-1}$  for BM03 and  $\sigma_{\text{ion}} = 1.6 \text{ mS cm}^{-1}$  for BM01 (cf Fig. S1). Particles of BM03 and BM01 are on average smaller, thus, the decreasing ionic conductivity compared to BM10 indicates a higher contribution of the ionic contact resistance between individual particles, which is in line with other reports of this material class.<sup>34,44</sup> There are no changes observable in the X-ray diffractograms of all three samples depicted in Fig. 1e, which display largely glassy or glass-crystalline materials with some LiI impurity.

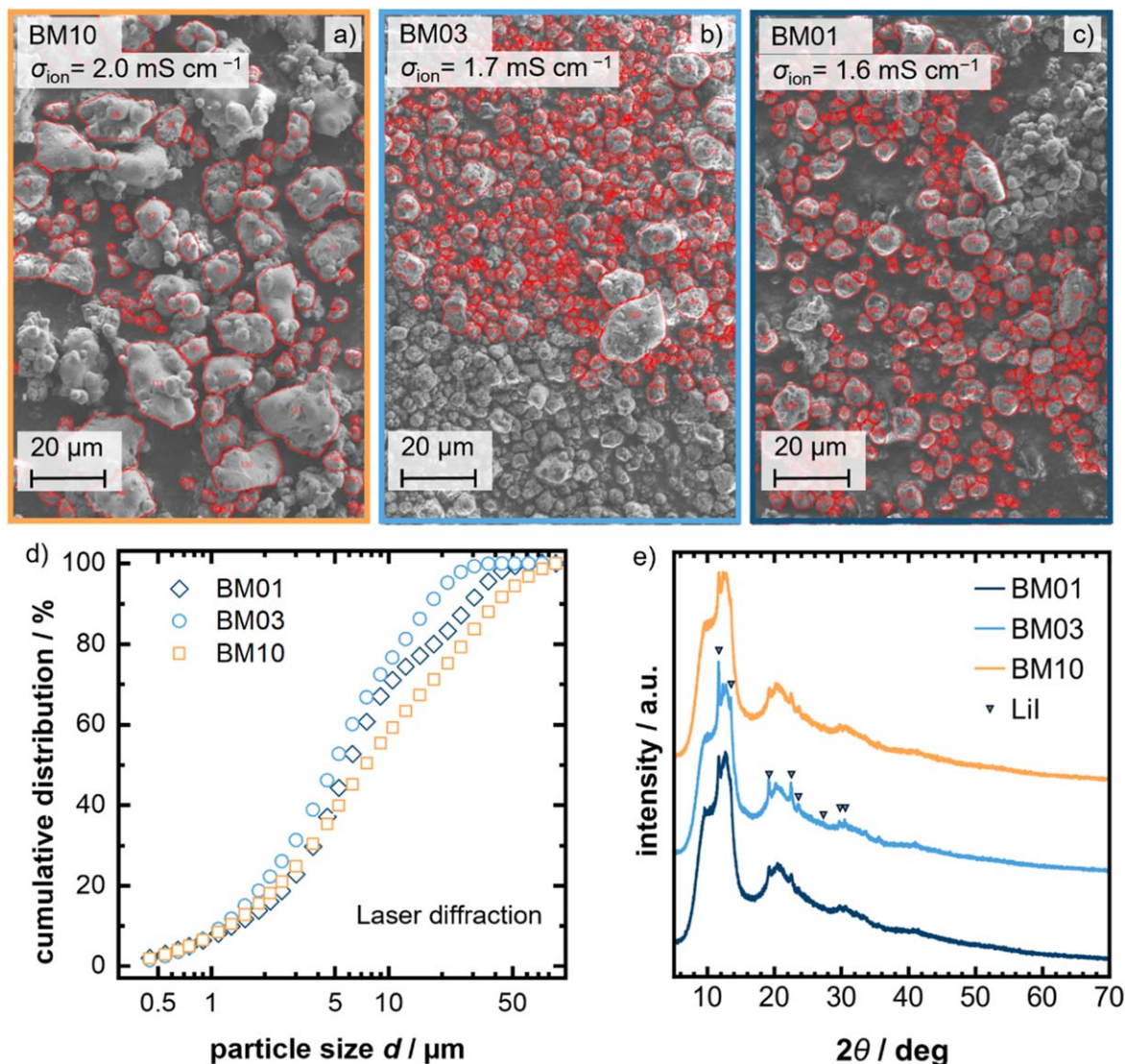


**Figure 1.** SEM images and analysis results of differently sized  $\text{Li}_3\text{PS}_4\text{-}0.5\text{LiI}$  solid electrolyte particles. Solid electrolytes were ball milled with (a) 10 mm (BM10), (b) 3 mm (BM03) and (c) 1 mm (BM01) milling media. Red boundaries indicate individual particles and were inserted manually. Smaller milling media lead to a reduction in particle size without significant loss of ionic conductivity. (d) Volume-weighted particle size distribution measured by laser diffraction. (e) XRD pattern of BM10, BM03 and BM01 samples showing characteristic patterns of glassy samples with some LiI impurity.

To investigate the influence of the different ISE particle sizes on cathode transport properties, we prepared composite electrodes by thoroughly mixing ISE and CAM. We subsequently determined the effective conductivities by impedance spectroscopy with two different experimental setups and corresponding transmission line models.

For the determination of the electronic partial conductivity, a composite electrode was embedded between two steel stamps that serve as current collector and block ionic transport. This cell concept known as *ion blocking electrodes* is typically used for mixed ionic-electronic conductors but can be applied to SSB cathodes, too.<sup>18,25,28</sup> While it is possible to determine the ionic conductivity from these impedance spectra, a large uncertainty exists, if ionic and electronic conductivity differ by orders of magnitude. Therefore, the ionic partial conductivity was measured in a different cell configuration, which we denote as *full blocking* (Fig. 2b), in which an ISE layer is sandwiched between two composite electrode layers. This setup has recently become increasingly popular in battery research.<sup>27,64,65</sup>

A transmission line model (TLM) is used to fit the impedance data of the composite electrode, i.e. the electronic and the ionic charge transport, and the interface between the two phases.<sup>66</sup>

Analogous to our previous work,<sup>18</sup> the use of fully lithiated NCM means that lithium ion transfer cannot take place between NCM and ISE due to the very high charge transfer resistance. T-type and Z-type TLMs (Fig. S2) correspond to the different cell setups as described below. Detailed explanations of these models and their physical meaning can be found elsewhere.<sup>66</sup> From the resulting fits, the charge transport resistances  $R_{cc}$ , (c.c. being the respective charge carrier—“e” for electronic and “ion” for ionic transport) were obtained, and the respective effective partial conductivities  $\sigma_{cc,eff}$  calculated according to Eq. 2:

$$\sigma_{cc,eff} = \frac{l}{R_{cc} \cdot A} \quad [2]$$

with the electrode thickness  $l$  and the cell area  $A$ . In the case of the electron blocking cell setup, the obtained resistance corresponds to the sum of both electrode layers, and for the determination of the partial conductivity, the resistance was divided by a factor of two.

Figures 2a and 2b show representative impedance plots of the electrodes together with the corresponding cell setups. In the spectrum of the ion blocking setup (Fig. 2a, a large semicircle is

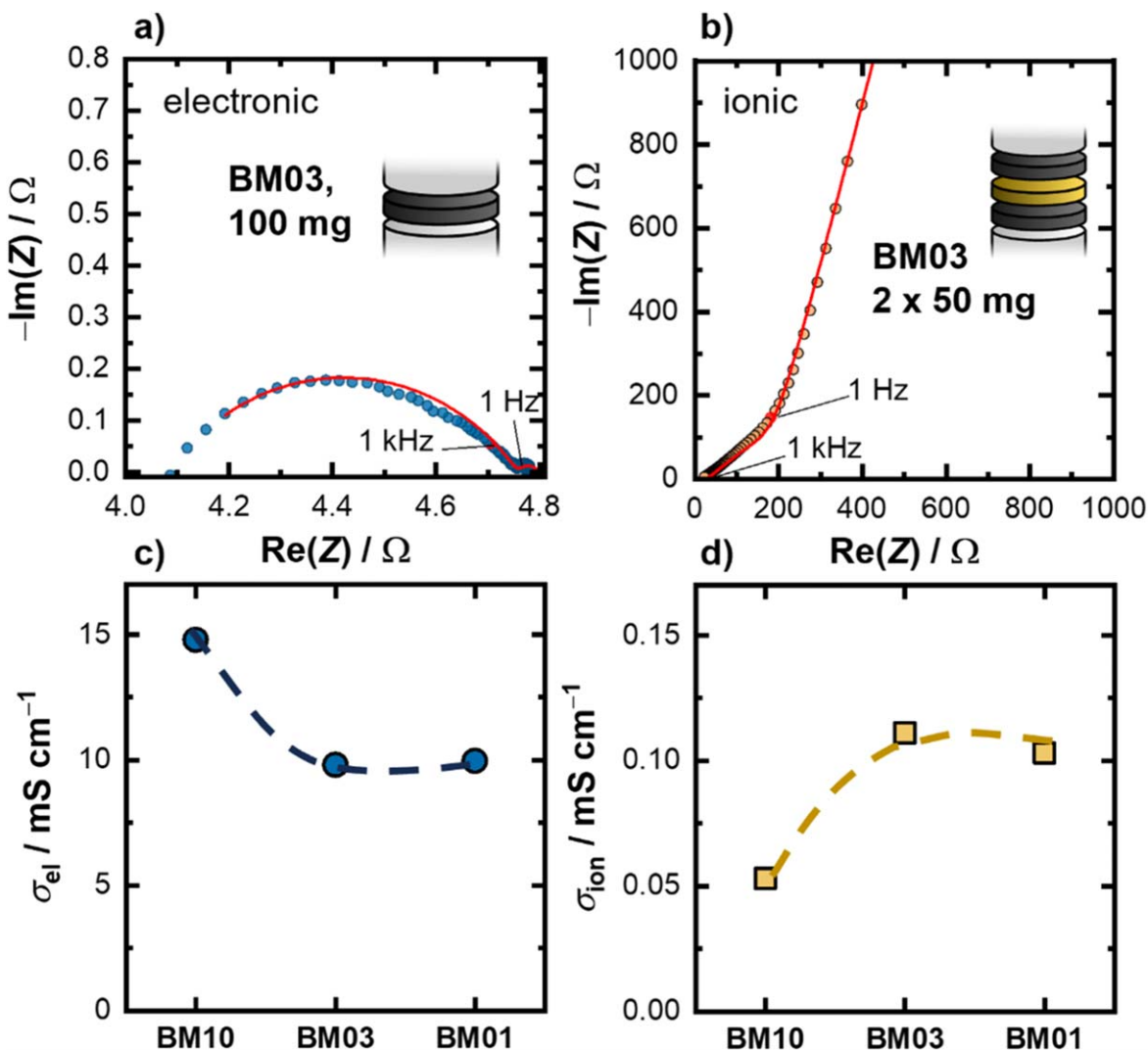


**Figure 2.** Evaluation of partial effective conductivities of composite cathodes containing 70 wt-% CAM and 30 wt-% ISE from impedance spectra using selectively blocking cell configurations. (a) Ion blocking cells (steellcathodelsteel) and respective impedance spectrum with fit (red line), and (b) full-blocking cell (steellcathodelsteel) and respective impedance spectrum with fit (red line). Effective conductivities of (c) electronic and (d) ionic charge carriers display an influence of the charge transport on the particle size of the solid electrolyte. While the effective electronic conductivity decreases with smaller ISE particles, the effective ionic conductivity increases, showing a more homogeneous distribution of both phases. Dashed lines are guides to the eye. Based on the uncertainty of the thickness determination, the influence of the applied pressure and the fit, we estimate the uncertainty of the data to be approx. 20%.

visible at high frequencies and a small semicircle is visible at low frequencies. At very low frequencies a purely resistive impedance can be observed. This shape is characteristic for T-type TLMs, in which two transport processes occur in parallel and in which one charge carrier is not blocked and can transfer across the current collector-sample interfaces. In contrast, the spectrum of the full blocking setup displays a 45° slope at high frequencies, which transitions into a much higher phase angle below 1 Hz. Such a shape is characteristic for a Z-Type TLM, in which interfaces are capacitive at low frequencies, which is the case for fully lithiated NCM.<sup>27,66</sup> In both cases, the employed models accurately fit the spectra with low residuals.

While  $\sigma_{\text{el,eff}}$  evidently decreases from 15  $\text{mS cm}^{-1}$  for the BM10 sample to around 10  $\text{mS cm}^{-1}$  for the BM03 and BM01 sample,  $\sigma_{\text{ion,eff}}$  increases by almost a factor of two, from 0.05  $\text{mS cm}^{-1}$  to 0.11  $\text{mS cm}^{-1}$  when using 3 mm instead of 10 mm milling media. This indicates improved ionic transport through the cathode and likely results from more and shorter ionic transport pathways and, thus, better percolation. The loss of  $\sigma_{\text{el,eff}}$  may be explained by reduced clustering of active material particles and therefore a better overall distribution, as discussed by Iwamoto et al.<sup>48</sup> CAM particle

clusters serve as electronic “highways” with low  $R_{\text{el}}$ , but they do not necessarily lead to lower overall cell resistance in full cells since particles inside the cluster have low contact areas to the ISE phase, which hinders charge transfer and blocks ionic transport on a micrometer scale, which is evident from the measured  $\sigma_{\text{ion,eff}}$  values. Similar phenomenological observations were already made by several groups for other thiophosphate-based ISEs. As there is yet no quantitative model for these effects, this needs further investigation.<sup>42,48</sup>

**ISE particle size determines cathode homogeneity and porosity.**—As we intend to evaluate how particle clusters and the microstructure influences the kinetics of composite electrodes, we employed Xe-plasma FIB-SEM (PFIB-SEM) to measure the three-dimensional microstructure of the three composite cathodes to a cubic voxel size of 100 nm. The images obtained from PFIB-SEM tomography were segmented into CAM, ISE and pore phases, based on gray scale values of both secondary electron (SE) and back-scattered electron (BSE) images (Fig. 3). Subsequently, the collected images were transformed to three-dimensional reconstructions, which were used to carry out digital microstructural analyses.

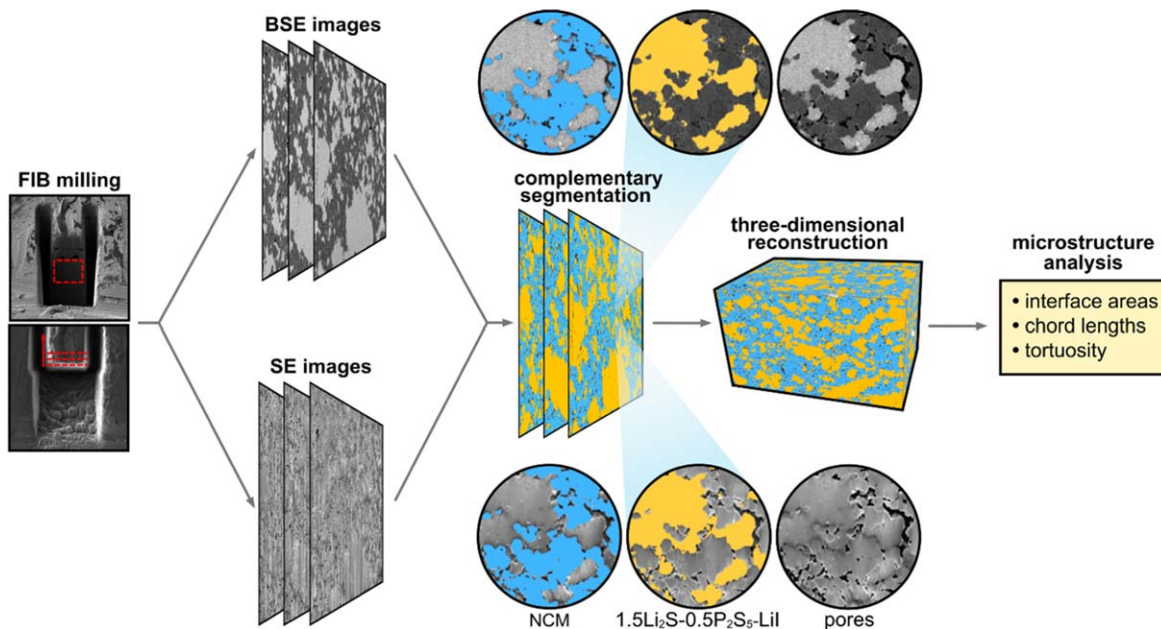


**Figure 3.** Schematic representation of the PFIB-SEM tomography procedure to obtain three-dimensional reconstructions of composite cathodes. After image acquisition, both BSE and SE images are used to assign CAM (NCM, blue), ISE ( $\text{Li}_3\text{PS}_4-0.5\text{LiI}$ , yellow) and pore (black) volumes.

Using only BSE images does not result in a sufficiently clear segmentation of pores as SEM is not a surface-sensitive technique and materials that lie lower than these pores contribute to the signal. In contrast, SE images depend more on surface topography, which makes it easier to detect pores as they are cavities in a finely polished flat surface. Details about the tomography parameters are shown in Sect. S2.

The respective segmented volume fractions are displayed at the same scale in Fig. 4a. Differences in external dimension of the three-dimensional reconstructions are due to the sample acquisition process. Figures 4b–4d show the volume fractions obtained from PFIB-SEM and the geometric volume fractions calculated from the original masses and densities of the employed materials and the outer dimensions of the samples (cf Sect. S4).

The nominal ratio of CAM:ISE phase by volume is about 50:50 for all three samples. However, the BM10 sample shows a segmented CAM amount of 55 vol-% and distinct deviations of the segmented CAM and ISE fractions to the expected ones. Deviations from the nominal ratio in the analyzed segmented and geometric volume fractions are mostly caused by small ISE particles and pores that are falsely attributed as CAM. As the overall pore fraction is larger in the BM10 microstructure, the deviation is more prominent than in BM03 and BM01. The ISE content can be detected reliably in the BM01 and BM03 samples as there is sufficient phase contrast in the BSE images. The discrepancy of segmented and geometric volume fraction affects the simulation of electric transport as discussed below.

The porosity determined by segmentation (segmented porosity) is much lower than the geometric porosity and is comparable to values typically reported for reconstructions of SSB cathodes.<sup>47,51</sup> The geometric porosity is in good agreement with other studies utilizing the density of the sample for porosity determination.<sup>18,53,67</sup> We attribute this discrepancy to pores falsely segmented as CAM and the presence of nanosized pores  $<50$  nm, which can form at the interface of the different particles and are typically not detected, unless a much higher SEM-resolution can be achieved.<sup>67</sup> A higher resolution would give more detail about the microstructure but would significantly increase measuring and computing time for processing the large data sets. While the exact nature, location and shape of the nanosized pores described above remains unresolved, we point out that they likely block charge transport and transfer in

the same way as larger pores do and so contribute to the overall charge transport resistance.<sup>33,53,68</sup>

Additionally, we assume some material redeposition to be present during PFIB-milling, which results in material deposits within the pores and reduces the detectable porosity. This leads to smaller values of segmented than geometric pore volume fractions. Still, there is a clear trend of decreasing porosity for samples with smaller ISE particle size in both analysis methods. Smaller ISE particles reduce the inhomogeneity of the microstructure as they are more likely to fit in between CAM particles, which reduces the porosity in areas of high CAM content.

In the next step we evaluate geometric descriptors of the obtained reconstructions to describe the microstructure of these cathodes quantitatively. We emphasize that we use geometric reconstructions of actual cathodes and do not generate digital twins by any statistical or stochastic methods. This allows a quantitative investigation of the “true” microstructure in a 3D model including phase distribution and local inhomogeneities.

Examples of these geometric descriptors are the chord-length (CL) and chord-length-distribution (CLD) which are measures of how far a specific phase protrudes towards a specific direction inside the sample without facing the boundary of another phase (Fig. 5b). A distribution at smaller CLs therefore corresponds to a more homogeneous distribution of the phases wherein the current is distributed more homogeneously, and bottlenecks are reduced compared to microstructures that feature larger CLDs. Figure 5a presents the CLD of the different samples.

In the CAM phase, a clear trend of reduced CLs for smaller ISE particle sizes can be observed, indicating a more homogeneous microstructure and less clustered CAM-particles. In the ISE phase, shorter CLs can be observed for the BM01 and BM03 samples, too, however, the BM01 sample shows a clear shift to lower CLs only at very small values  $<0.5$   $\mu\text{m}$ . The BM10 sample, on the other hand, possesses many larger ISE CLs  $>10$   $\mu\text{m}$ , which is a result of both, large ISE particles and ISE particle clustering.

In general, the trend towards smaller CLs corresponds to smaller ISE and CAM particle clusters and higher homogeneity of the cathode composite for the samples that were ball milled with smaller milling media (BM01 and BM03). Another important descriptor that indicates how a respective phase is distributed is the interface area  $S_{a-b}$  between two phases a and b (with  $a \neq b$ , e.g. the active interface

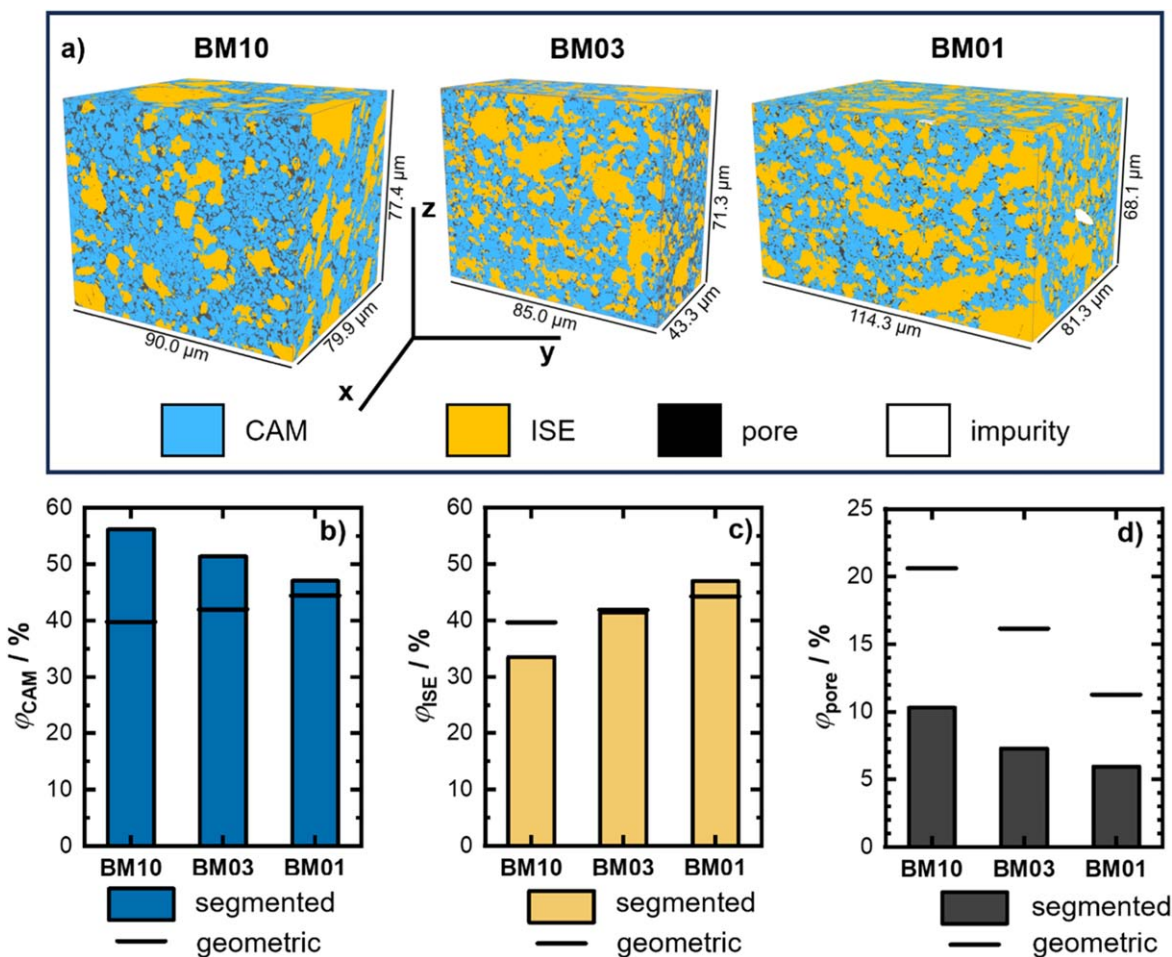


**Figure 4.** Segmented 3D reconstructions of cathode composites containing solid electrolyte that was treated with differently sized milling media. (a) Abbreviations indicating the employed milling media diameter: BM10 = 10 mm, BM03 = 3 mm, BM01 = 1 mm). All reconstructed volumes feature a voxel size of 100 nm. The reconstructed volume is segmented, and the corresponding volume fractions are determined for (b) CAM (NCM), (c) ISE ( $\text{Li}_3\text{PS}_4-0.5\text{LiI}$ ) and (d) pores. Black horizontal bars indicate the expected values calculated with the employed masses, the material density, and the porosity determined from geometric dimensions of the sample.

between CAM and ISE,  $S_{\text{CAM-ISE}}$ ). If particles of the same phase form clusters, only part of the surface area of the particles is available for interfaces with other phases and  $S_{a-b}$  is reduced. The interface area between CAM and ISE is of particular importance for the cell performance, as this is where the transfer of lithium ions takes place. To allow for a low charge transfer impedance, a high interface area is required.

Figure 5c shows, that, compared to BM10, the BM03 and BM01 samples exhibit a larger contact area between CAM and ISE. Thus, less pores are in contact with the CAM and  $S_{\text{CAM-pore}}$  is decreasing from  $0.34 \text{ m}^2 \text{ g}^{-1}$  for BM10 to  $0.16 \text{ m}^2 \text{ g}^{-1}$  for BM01, while simultaneously,  $S_{\text{CAM-ISE}}$  increases from 0.11 to  $0.24 \text{ m}^2 \text{ g}^{-1}$ . This observation can be explained by smaller CAM clusters. Voids between individual CAM particles can be filled by the smaller sized ISE during fabrication<sup>48</sup> as already observed in the measured total porosity. This penetration of pore space between CAM particles goes hand in hand with shorter diffusion lengths for lithium ions and better kinetics.<sup>68</sup> Assuming a specific surface area of  $0.5 \text{ m}^2 \text{ g}^{-1}$  for the CAM (as given by the supplier), this implies that the coverage of CAM particles by ISE increases from around 20% for BM10 to almost 50% for BM03 and BM01. However, half of the CAM surface area is still covered by pores (31%) and other CAM particles (19%). The high accumulation of pores at the interface can significantly affect the performance of the cathode as current constriction phenomena and high interfacial resistances will increase the overall cell resistance.<sup>68</sup> We point out, that the overall porosity of

the sample is smaller for BM03 and BM01 than for BM10, which is in line with the results described above as ISE particles of reduced size can fill smaller void spaces.

Interestingly,  $S_{\text{ISE-pore}}$  increases upon ISE particle size reduction from  $0.05$  to  $0.09 \text{ m}^2 \text{ g}^{-1}$  as well, which we assume to be caused by more point-to-point contacts between the respective ISE particles. The fact that the  $S_{\text{ISE-pore}}$  values are in general much smaller than the  $S_{\text{CAM-pore}}$  values can be explained by the mechanical properties of the employed materials.<sup>50</sup> The rigid CAM particles<sup>69</sup> tend not to deform significantly during densification, hence, any porosity between CAM particles cannot be closed, while the much more malleable ISE<sup>70,71</sup> allows for the removal of pores between individual ISE particles.

We conclude that a homogeneous distribution of the different phases, supported by small ISE particles, is crucial for homogeneous composite cathodes with high  $S_{\text{CAM-ISE}}$  and low residual porosity. Sophisticated processing and careful selection of materials with matching properties are very important to produce cathodes that can deliver fast kinetics, as we present and discuss in the following chapter.

#### Charge transport is determined by microstructure.—

Complementary to geometric descriptors, we carried out charge transport simulations to correlate microstructure and transport kinetics. The tortuosity factors  $\kappa_a$  of a respective phase a can be determined by comparison of the effective conductivities  $\sigma_{a,\text{eff}}$  to the



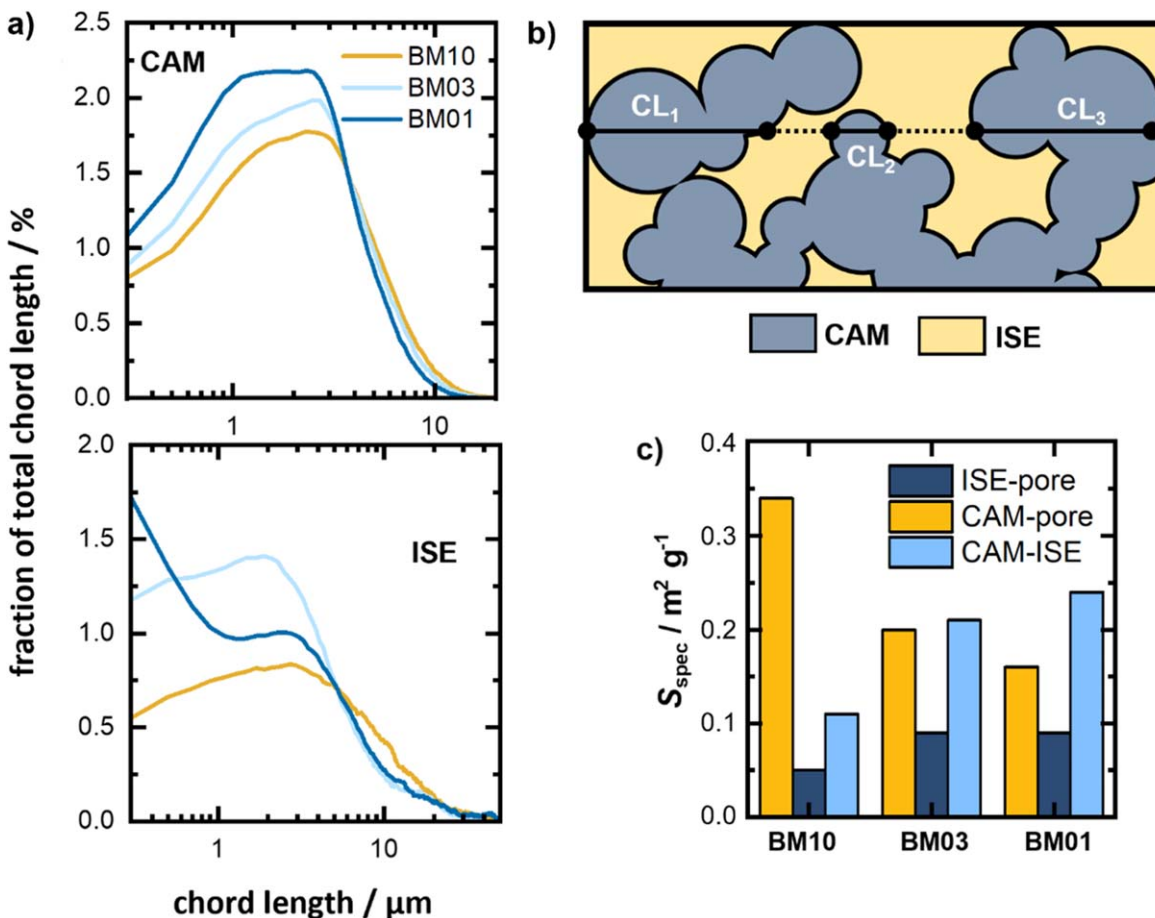


**Figure 5.** Microstructural descriptors obtained from analyzing the reconstructed microstructure of the composite cathodes. (a) CAM phase showing smaller clusters for cathodes with smaller ISE particles and SE phase showing significantly reduced particle clusters  $>10 \mu\text{m}$ . (b) Chords describe 1D protrusion of phases and the respective length distribution can be determined for the different phases. Total chord length resembles the sum of all chord lengths. (c) Specific interface area between the different phases showing a clear dependence on the ISE particle size.

bulk expected conductivity  $\sigma_{a,\text{bulk}}$  and the phase fraction  $\phi_a$ , according to Eq. 3

$$\kappa_a = \frac{\sigma_{a,\text{bulk}}}{\sigma_{a,\text{eff}}} \phi_a \quad [3]$$

Alternatively, tortuosity factors can be approximated by random walk simulations which use diffusion transport equations or by flux-based simulations. Compared to random walks, flux-based simulations are in general more applicable to electrochemical transport data because they also consider “dead ends,” and have already been employed in several studies on SSB composites.<sup>15,35,72–75</sup> In this study, we use both approaches and compare the obtained tortuosity factors to the values determined from experimental data (Fig. 6).

In the ion-flux simulation (Fig. 6a), inhomogeneous transport is observed in the BM10 sample, while for the BM03 and BM01 sample, the charge transport pathways appear more homogeneously distributed.<sup>15,35</sup> Local “hotspots” i.e. regions of very high current density are less pronounced, showing reduced bottlenecks for the ions to flow through. It is therefore expected that the cathode is more evenly (dis)charged throughout its thickness. These results support the findings of Schlautmann et al. who also used flux-based simulations of artificially generated microstructures with different ISE particle size and compared these to experimental observations.<sup>72</sup> Our approach, therefore, strengthens the conclusions of more homogeneous cathodes by smaller ISE particle sizes.

The tortuosity factors (Fig. 6b) can be calculated for electronic as well as ionic transport and should be as low as possible in order to provide short charge transport pathways. It is important to note

that the concept of tortuosity factors is, although useful for battery research, still under debate and tortuosity factors are not necessarily a sufficient way to quantify microstructures, especially if these are heterogeneous in nature.<sup>76</sup> However, they are suited for a qualitative assessment of the microstructural influence of the particle size. To motivate further investigations and the development of more suited descriptors in future studies, we provide the obtained raw tomography data as **supplementary datafiles** (<http://dx.doi.org/10.22029/jpub-18458>).

While the experimental electronic tortuosity factor  $\kappa_{e,\text{exp}}$  of the BM10 sample is around three, the calculated ones are below two, which is comparable to values reported for LIB electrodes.<sup>22</sup> The cathodes in commercial LIBs, however, are conceptually different: the volume fraction of the CAM is significantly larger than in the composite electrodes of this work, and they contain carbon additives for enhanced electronic conduction. While these factors should result in lower electronic tortuosity factors than in the present study, LIB cathodes usually also contain polymeric binders, that impede charge transport. We note that only little influence of the particle size can be seen in terms of  $\kappa_{e1}$ , especially in the simulated data.

For all samples, we observed that the random walk as well as the flux-based simulations lead to almost identical values, which means, that no major bottlenecks or dead ends lower the conductivity. The experimental ionic tortuosity factor  $\kappa_{i,\text{exp}}$  is around 15 for the BM10 sample - more than five times higher than the electronic one, highlighting the inhomogeneity of the sample and the poorly distributed ISE. However,  $\kappa_{i,\text{exp}}$  decreases to around six (four for the simulation) in the samples with smaller ISE particles, which is in

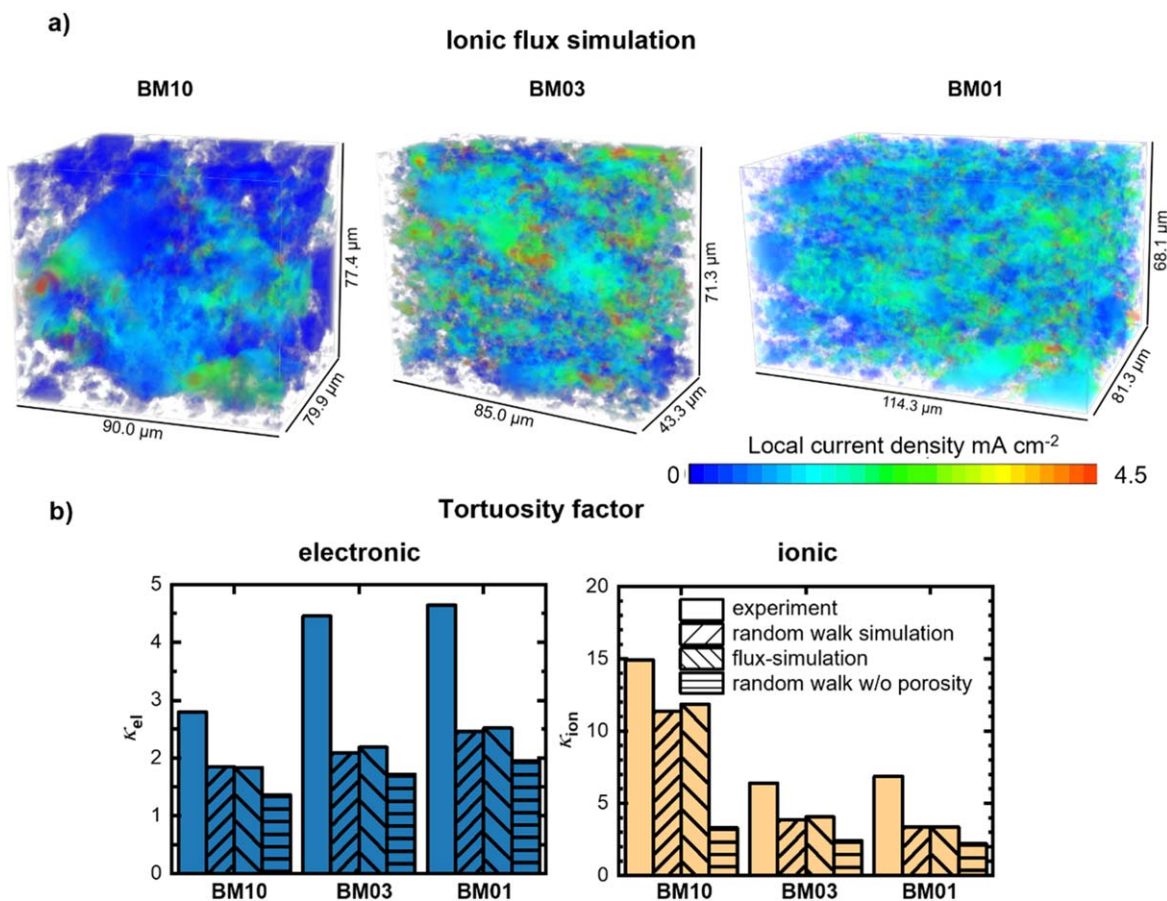


**Figure 6.** Simulation results of ionic-flux and comparison of experimentally determined and simulated tortuosities. (a) Ionic flux-distributions simulated for the three microstructure reconstructions with different ISE particle size. (b) Tortuosity factors of electronic and ionic transport determined from impedance spectra and from charge transport simulations on the reconstructed microstructures. A significant improvement of the ionic transport is visible for smaller ISE particles. Large differences between experimental and simulated charge transport indicate an influence of segmented porosity and particle-particle contact resistances.

line with the observation of a better distribution of ISE particles and a correspondingly homogenized microstructure. Note that the simulated tortuosity factors are, in general, very similar for all three dimensions in all reconstructions, except for  $\kappa_{\text{ion}}$  in the BM10 sample, which is significantly increased along the  $x$ -axis (cf Fig. S6). We attribute this observation to the presence of large CAM clusters, which effectively block the ionic transport along this direction.

In general,  $\kappa_{\text{el}}$  are lower than corresponding  $\kappa_{\text{ion}}$ . The experimentally obtained values are much higher than the calculated ones for both charge carriers. We assume that this discrepancy of experimental and simulated values is due to several reasons:

- I. Contact resistances between the current collectors and the electrodes, and grain boundaries lower the determined conductivity<sup>77</sup> but cannot be resolved in our microstructure reconstructions.
- II. Nanopores, that influence particle-particle contacts reduce the effective conductivity by current constriction but are not resolved in the SEM images and the resulting segmentation.<sup>67</sup>
- III. Current constriction phenomena, that influence the total current distribution and disrupt the homogeneity of the electric field, leading to overpotentials are not considered. Additionally, high local current densities can result in high local temperatures and especially in case of narrow bottlenecks in a stronger degradation between ISE and CAM.

While these individual effects, or a superposition of them, can play a role for ionic transport, electronic transport or both, the general trend of improved ionic transport at reduced ISE particle

sizes is reflected by both simulation and experiment. The increase in the electronic tortuosity with decreasing ISE particle size can be explained by the fact that these small ISE particles, can effectively break up CAM clusters, which slightly decreases effective electronic conductivity while simultaneously improving ionic conductivity. This observation is well in line with previous reports.<sup>18,48</sup>

As discussed above, porosity is an important factor impeding charge transport and transfer. Its influence was tested using random walk simulations in which transport properties of either the ISE or the CAM phase were attributed to the segmented porosity given. That allowed us to investigate the tortuosity factors that are theoretically attainable in a completely densified sample. Results are displayed in Fig. S7. Clearly, the “filling” of porosity has a significant effect on the ionic charge transport, while the effect on electronic transport is rather small. This observation is a strong indication for pores being predominantly present in CAM clusters, therefore preventing ionic transport in these areas. There is, however, no significant influence of the ISE particle size on the “pore-less” tortuosity factor, showing, that the porosity is the main inhibitor of the charge transport, and that the main contribution of the ISE particle size is on the homogeneity and reduction of porosity in SSB cathodes. Additionally, the results show, that with proper processing techniques that allow for full densification, i.e. warm isostatic pressing, tortuosity factors comparable to the ones of LIBs could be achieved, which is in line with recent experimental findings by Koenig et al.<sup>39</sup>

Overall, our observations demonstrate that the residual porosity is particularly harmful for the ionic transport, which is already a limiting factor, and we assume that pores would be even more severe

in cathodes with higher CAM contents. Ultimately, charge transport must be tailored by particle size and strategies to reduce porosity and increase the effective ionic conductivity.

**Homogeneous microstructures are necessary to improve cell performance.**—SSB cells with cathodes featuring the three different ISE samples were investigated with In/(InLi)<sub>x</sub> alloy and Li<sub>6</sub>PS<sub>5</sub>Cl as anode and separator material, respectively. Galvanostatic cycling was performed within the voltage range of 2.62–4.32 V vs Li<sup>+</sup>/Li for different C-rates to evaluate the kinetic influence of the microstructure of the cathode. It is important to mention that similar mass loadings and identical masses for the separators and anodes were used. The discharge capacities of the galvanostatic cycling are presented in Fig. 7a.

We find that the BM10 sample, which features large sized SE particles, performs much worse than the other two samples at low as well as at high C-rates: the sample achieves capacities of 92 mAh g<sup>-1</sup> at 0.1 C, compared to 152 and 156 mAh g<sup>-1</sup> for the BM01 and BM03 cells, respectively. This correlates well to findings by Shi et al.<sup>34</sup> and Schlautmann et al.<sup>72</sup> and is clearly showing the detrimental influence of the large SE particles on the microstructure. Similar information can be drawn from the *dQ/dV* plot (Fig. 7b), where the characteristic peaks of the CAM material are less explicit for BM10 compared to BM03 and BM01 curves. For the H2/H3 phase transition, this is a result of slower kinetics, caused by overall longer transport pathways. Additionally, the delayed onset of the “kinetic hindrance” peak is an indication for overall increased overpotentials, which can be correlated to the ionic

tortuosity and the lower values in *S*<sub>CAM-ISE</sub>. With increasing C-rates, the capacity drops further, which can be attributed to higher overpotentials, as shown in Figs. 7c and 7d. At 1 C, we find that for BM10 only 25% of the initial low C-rate capacity are retained, compared to 28% and 32% for BM01 and BM03, respectively. While this shows severe kinetic issues in the composite cathode, the sum of the results demonstrates the positive influence that homogeneous conduction pathways can have on the cell kinetics. At low C-rates, the influence of kinetics on the measured cell voltage is reduced and the total mass of electrochemically connected material, i.e. the material having access to percolating electronic and ionic charge transport pathways, determines the achievable capacity. In contrast, at high C-rates kinetics have a larger impact and the length of these pathways and, thus, the overpotential caused by their resistance dominates the capacity.<sup>18</sup> The low C-rate performance can be used as an identifier of significant inhomogeneities of the microstructure, while the high C-rate performance is an indication of the tortuosity of charge transport pathways and low interfacial contact between CAM and ISE.

Please note, that additional processes contribute to the full cell kinetics, i.e. the anode kinetics, charge transfer resistance at the interface between CAM and ISE, which depends on *S*<sub>CAM-ISE</sub> and the exchange current density. This is an additional process contributing to the poor performance of cells with large ISE particles.<sup>68</sup>

Interestingly, the 1st cycle *Coulomb* efficiency at 0.1 C (Fig. S8) is much higher for the BM03 and BM01 samples ( $\eta = 73\%$  and  $68\%$ ) compared to the BM10 sample ( $\eta = 58\%$ ) even though the higher interface area of the former samples results in more severe

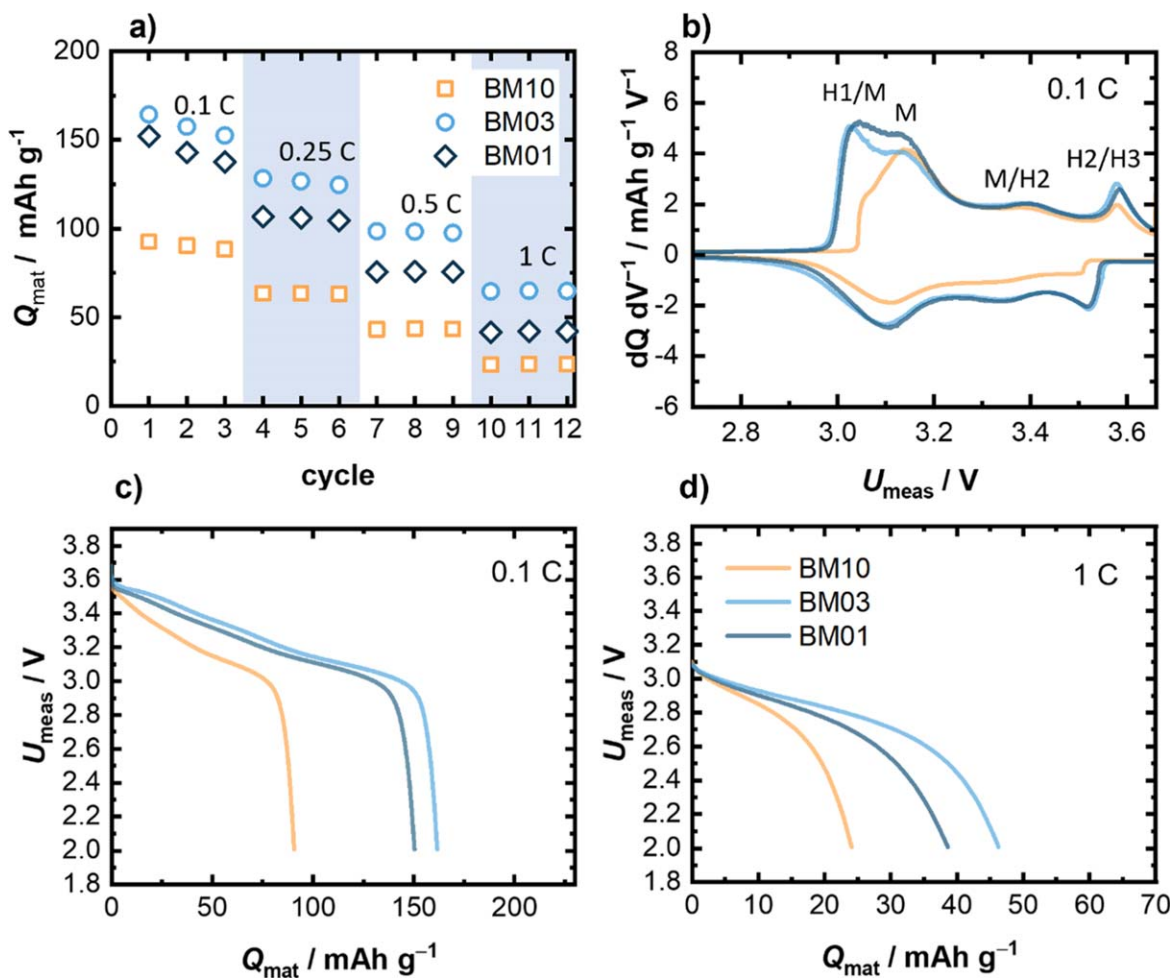


**Figure 7.** Electrochemical cycling performance of the analyzed cathodes in full cell configuration. Full cells were constructed using InInLi anodes and a mass loading of 10.7 mg cm<sup>-2</sup>. (a) Discharge C-rate capability, (b) differential capacity at 0.1 C and discharge curves of cells at (c) 0.1 C and (d) 1 C. Large ISE particles result in reduced capacity due to slower kinetics and higher overpotentials as well as particle clusters that reduce the charge transfer capabilities.

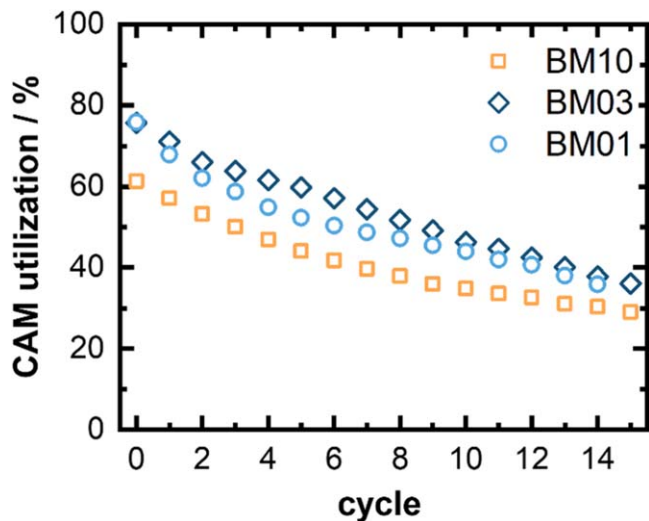


**Figure 8.** CAM utilization as a function of cycle number. Utilization was calculated by determining the active mass of the CAM phase. A much lower level of CAM utilization is observed for cathodes with large ISE particles showing the extent to which CAM clusters affect the electrochemical performance.

degradation. We attribute low *Coulomb* efficiency determined for all samples to interfacial degradation and chemo-mechanical losses within the first cycle.<sup>78</sup> These result from contact loss at the CAM-ISE interface<sup>51,79</sup> due to expansion and contraction of CAM particles during (dis-)charge, which are more severe in case of the BM10 sample as there are already smaller  $S_{\text{CAM-ISE}}$  values.

Overall, the data obtained from the electrochemical performance is consistent with the information obtained from the segmentation, i.e.  $S_{\text{CAM-ISE}}$ , as well as with the simulated and measured tortuosity factors of the cathodes. Our results are, therefore, a clear indication that small SE particle sizes improve the cell performance, as they enable more homogeneous microstructures with favorable transport properties. Observations of improved cell performance for small ISE particles have also been made by Shi et al.,<sup>34</sup> Cronau et al.<sup>44</sup> and Schlautmann et al.<sup>72</sup> Comparing our results with the findings of both studies and using the proposed particle size ratio of CAM and ISE, i.e.,  $\lambda = d_{\text{CAM}}/d_{\text{ISE}}$ , we find that BM10 with  $\lambda = 0.7$  and BM03/BM01 with  $\lambda = 1.0$ – $1.2$  perform well within the predictions of this model. A low amount of electrochemically accessible material, which we denote as CAM utilization, in line with Bielefeld et al.<sup>14</sup> and Shi et al.,<sup>34</sup> is therefore the reason for the poor performance of the BM10 cells.

**Smaller ISE particles lead to higher CAM utilization.**—To further quantify the influence of the microstructure on loss of CAM utilization, we adapted the methodology of Ruess et al.<sup>80</sup> to determine the electrochemically active mass. This method utilizes a comparative measurement of the open circuit potential (OCP) in equilibrium as a function of lithium content and the relaxed OCP after (dis-)charge. Electrochemically inactive particles do not contribute to (dis-)charge processes and, respectively, not to the OCP of the cell. Details can be found in Fig. S9. The determined electrochemically active masses for 15 consecutive cycles allows to evaluate the chemo-mechanical degradation caused by the contact loss between CAM and ISE. The results are presented in Fig. 8.

Comparing the initial CAM utilization, we find that within the BM10 sample only 62% of the CAM mass is electrochemically active, which is an explanation for the low overall capacity that can be achieved. In contrast, the BM03 and BM01 samples exhibit significantly larger values of 77% CAM utilization. The visualization of the electronic conduction clusters of the reconstructed microstructures (cf Fig. S10) does not indicate a significant number of isolated CAM particles. Still, the experimentally determined

utilization level indicates an increased clustering in BM10 resulting in a disconnection of CAM clusters from the ion percolating network. Consequently, a more pronounced CAM clustering due to larger ISE particles may lead to a reduced active mass. In contrast to the CAM network, however, the ISE network shows a clear increase for decreasing  $d_{\text{ISE}}$ , which may suggest a more important role of ionic percolation on the CAM utilization. These results are in line with Shi et al.<sup>34</sup> whose model showed a decrease of the percolating ISE network for increasing  $d_{\text{ISE}}$ , which led to a reduced fraction of CAM particles in direct contact with the ISE.

We assume the reduction of active mass is mainly caused by CAM particles close to the current collector without contact to the ionically percolating ISE network, as for these particles, ionic conduction paths are already much longer. These regions are included in the tomography data presented in this study. An additional aspect causing a reduced active mass in BM10 may be the smaller electrochemically active interface area as discussed above.

It is important to note that these conclusions are based on the reconstructed volume of pristine composites. Electrochemical cycling induces irreversible alterations of the microstructure, i.e. decomposition reactions<sup>81</sup> and chemo-mechanical volume changes of constituents can cause disconnections of CAM particles from the percolating network and an increase in porosity.<sup>51</sup> Significant capacity fading, particularly in the first cycle, was reported for thiophosphate-based ISE and was linked to a formation of high resistive interphases, which can lead to an insulation of CAM particles, as well as contact loss between CAM and ISE due to the contraction of CAM particles upon charging.<sup>54,78</sup>

Interestingly, during cycling all samples show a similar loss of active material and no clear trend can be observed regarding the influence of  $d_{\text{ISE}}$ . The decrease in CAM utilization can be explained by contact loss at the interface between CAM and ISE, effectively reducing the charge transfer sites. Additionally, mechanical fatigue mechanisms such as cracking within the single-crystalline CAM aggregates can lead to electronically isolated particles, that do not participate in the electrochemical cycling anymore. However, there seems to be no significant influence of  $d_{\text{ISE}}$  and we assume that the contact loss mentioned above takes place in CAM clusters, as well as in well distributed particles. A more detailed investigation of  $d_{\text{ISE}}$  on the role of chemo-mechanics, i.e., on the pressure evolution during cycling, however, is beyond the scope of this study and will be part of future investigations.

**Shortcomings of this study and remaining challenges in cathode optimization.**—Beyond the results discussed above, our study reveals the difficulties in reliably determining the porosity of composite cathodes for SSBs. First, the geometric porosity and the segmented porosity differ significantly, which affects the charge transport properties. Even with highly resolved PFIB-SEM images it is not always possible to detect pores by gray scale contrast. Since a detailed understanding of the microstructure can only be achieved if the resolution is higher than the smallest particle/pore size, it is essential to achieve a resolution in the range of 100 nm, as has been used in our study. This requires either synchrotron-based or electron beam-based techniques both of which are rather expensive and require a higher degree of automatization in order to obtain tomography data of large volumes of multiple samples.

Additional to the image acquisition, the processing of tomography data needs improvement. More sophisticated and more efficient image processing techniques are necessary. Considering the large amount of data (gigabytes of images that have to be segmented automatically) that need to be processed, machine learning algorithms could help to better segment images and to help understand the microstructure of composite cathodes.

Our study could not resolve the reason for the decreased (effective) conductivity of smaller ISE particle networks unequivocally, and a segmentation of particle contacts was not possible. In future work, these particle-particle interfaces need to be considered for charge transport and electrochemical simulations. This could be

achieved either by a more sophisticated sample preparation, such as etching, or by artificially introducing these boundaries in a model based on the particle size distribution of the employed powders.<sup>77</sup> In any case, the grain boundary “design” of electrolytes with very high bulk conductivity appears to be necessary.

We showed that the residual porosity is still present in cold pressed composite cathodes and most likely responsible for the poor electrochemical performance of the composite cathodes. It is worth noting, that all electrochemical experiments were conducted under comparably high pressures, which is necessary to properly operate this type of SSBs. In contrast, image acquisition was performed under high vacuum conditions. We assume the pressure to have an influence on the microstructure, however the pressure will most likely result in decreased porosity, and contact resistance. Based on our results it is, therefore, even more necessary to densify SSB components and to optimize the charge transport of composite cathodes.

A careful selection of particle size distributions, mixing and densification techniques are crucial for reducing porosity to a minimum. Warm isostatic pressing is a promising option and has previously been used for full densification of well-performing cathodes.<sup>8</sup> Additionally, conductive additives, such as plastic polymer or liquid electrolytes could fill residual pores and contribute to the kinetics of the cathode, but these concepts have rarely been employed and need further investigation regarding practicability, also regarding the (chemical) stability of interfaces. These concepts of “hybridization” may be chemically difficult for sulfide-type SEs, as they tend to dissolve easily in polar solvents (and polymers),<sup>82,83</sup> thus causing the risk of severe chemical instability.

Besides porosity, carbon additives will influence the percolation and tortuosities. Since they are electronic conductors, a beneficial effect on the electronic tortuosity is expected, however as they are another non-ion conducting phase, they will most likely impede ionic charge transport and transfer. Their use should therefore be limited, especially if high CAM contents are used. Also, carbon additives are an additional source of SE degradation at high potentials, as first reported by Zhang et al.<sup>84</sup>

## Conclusions

In this study, we analyze the three-dimensional microstructure of composite cathodes employing a sulfide-type ISE and a transition metal oxide-based CAM by FIB-SEM tomography and subsequent reconstruction. By varying the ISE particle size, we elucidate its direct influence on important microstructural descriptors and find correlations of these with the electrochemical data. A comparison of simulated and experimentally determined charge transport data shows that in microstructural modelling the effective conductivities are overestimated and tortuosities are underestimated. This is because the simulations rely on reconstructed microstructures that fail to reproduce the porosity values that are geometrically expected. The residual porosity plays a critical role in solid-state cathodes and additionally particle-particle contacts need to be considered. We further quantify the influence of the microstructure by analyzing the electrochemical performance of full cells. Based on our results, we conclude that small ISE particles are essential to obtain homogeneous cathodes, high interface area between CAM and ISE, low ionic tortuosity, and consequently, improved cycling and rate performance. The corresponding kinetic cell data highlight the necessity of optimizing the microstructure of cathodes for achieving solid-state batteries with high energy and power density. We hope that our results motivate further efforts in optimizing cathode microstructures by particle size adjustment, as well as investigations on the densification of cathodes by consolidation or the use of pore filling additives.

## Acknowledgments

We acknowledge financial support within the FestBatt Cluster of Competence (BMBF, Bundesministerium für Bildung und Forschung) in the projects 03XP0177A, 03XP0430A, 03XP0346D, 03XP0428E,

as well as the ProGral project (03XP0427). A.B. acknowledges financial support by the Hessian Ministry of Higher Education, Research, and the Arts (HMWK).

## Author Contributions

Conceptualization, P.M. and J.S., Methodology, P.M., J.S., Formal Analysis, P.M., J.S., S.K., A.B., Investigation, P.M., J.S. Re.R., Resources, S.B., J.J., Writing—Original Draft, P.M., J.S., Writing—Review & Editing, P.M., J.S., A.B., F.H.R., J.J., Funding Acquisition, S.B., J.J., Supervision, S.B., Ra.R., A.B., J.J., P.M. and J.S. contributed equally to this work.

## Declaration of Interests

The authors declare no competing interests.

## ORCID

Philip Minnmann  <https://orcid.org/0000-0002-9646-0487>  
 Johannes Schubert  <https://orcid.org/0009-0003-3148-6672>  
 Sascha Kremer  <https://orcid.org/0009-0009-3739-8749>  
 Anja Bielefeld  <https://orcid.org/0000-0003-2193-8375>  
 Jürgen Janek  <https://orcid.org/0000-0002-9221-4756>

## References

- J. Janek and W. G. Zeier, “A solid future for battery development.” *Nat. Energy*, **1**, 1167 (2016).
- M. Weiss et al., “Fast charging of lithium-ion batteries: a review of materials aspects.” *Adv. Energy Mater.*, **11**, 2101126 (2021).
- J. Janek and W. G. Zeier, “Challenges in speeding up solid-state battery development.” *Nat. Energy*, **8**, 230 (2023).
- T. Famprikis, P. Canepa, J. A. Dawson, M. S. Islam, and C. Masquelier, “Fundamentals of inorganic solid-state electrolytes for batteries.” *Nat. Mater.*, **1278** (2019).
- Y. Kato, S. Hori, T. Saito, K. Suzuki, M. Hirayama, A. Mitsui, M. Yonemura, H. Iba, and R. Kanno, “High-power all-solid-state batteries using sulfide superionic conductors.” *Nat. Energy*, **1**, 652 (2016).
- N. Kamaya et al., “A lithium superionic conductor.” *Nat. Mater.*, **10**, 682 (2011).
- S. Randau et al., “Benchmarking the performance of all-solid-state lithium batteries.” *Nat. Energy*, **5**, 259 (2020).
- Y.-G. Lee et al., “High-energy long-cycling all-solid-state lithium metal batteries enabled by silver-carbon composite anodes.” *Nat. Energy*, **5**, 299 (2020).
- J. Doux, H. Nguyen, D. H.-S. Tan, A. Banerjee, X. Wang, E. A. Wu, C. Jo, H. Yang, and Y. S. Meng, “Stack pressure considerations for room-temperature all-solid-state lithium metal batteries.” *Adv. Energy Mater.*, **10**, 1903253 (2020).
- D. H.-S. Tan et al., “Carbon-free high-loading silicon anodes enabled by sulfide solid electrolytes.” *Science*, **373**, 1494 (2021).
- X. Yang, K. Doyle-Davis, X. Gao, and X. Sun, “Recent progress and perspectives on designing high-performance thick electrolytes for all-solid-state lithium batteries.” *eTransportation*, **11**, 100152 (2022).
- G. Deysher, P. Ridley, S.-Y. Ham, J.-M. Doux, Y.-T. Chen, E. A. Wu, D. H.-S. Tan, A. Cronk, J. Jang, and Y. S. Meng, “Transport and mechanical aspects of all-solid-state lithium batteries.” *Mater. Today Phys.*, **24**, 100679 (2022).
- P. Minnmann et al., “Designing cathodes and cathode active materials for solid-state batteries.” *Adv. Energy Mater.*, **12**, 2201425 (2022).
- A. Bielefeld, D. A. Weber, and J. Janek, “Microstructural modeling of composite cathodes for all-solid-state batteries.” *J. Phys. Chem. C*, **123**, 1626 (2019).
- A. Bielefeld, D. A. Weber, and J. Janek, “Modeling effective ionic conductivity and binder influence in composite cathodes for all-solid-state batteries.” *ACS Appl. Mater. Interfaces*, **12**, 12821 (2020).
- A. Sakuda, T. Takeuchi, and H. Kobayashi, “Electrode morphology in all-solid-state lithium secondary batteries consisting of  $\text{LiNi}_{1/3}\text{Co}_{1/3}\text{Mn}_{1/3}\text{O}_2$  and  $\text{Li}_2\text{S-P}_2\text{S}_5$  solid electrolytes.” *Solid-state Ion.*, **285**, 112 (2016).
- A. Sakuda, “Favorable composite electrodes for all-solid-state batteries.” *J. Ceram. Soc. Jpn.*, **126**, 675 (2018).
- P. Minnmann, L. Quillman, S. Burkhardt, F. H. Richter, and J. Janek, “Editors’ choice—quantifying the impact of charge transport bottlenecks in composite cathodes of all-solid-state batteries.” *J. Electrochem. Soc.*, **168**, 040537 (2021).
- F. L.-E. Usseglio-Viretta et al., “Resolving the discrepancy in tortuosity factor estimation for li-ion battery electrodes through micro-macro modeling and experiment.” *J. Electrochem. Soc.*, **165**, A3403 (2018).
- T.-T. Nguyen, A. Demortière, B. Fleutot, B. Delobel, C. Delacourt, and S. J. Cooper, “The electrode tortuosity factor: why the conventional tortuosity factor is not well suited for quantifying transport in porous li-ion battery electrodes and what to use instead.” *NPJ Comput. Mater.*, **6**, 123 (2020).
- J. Landesfeind, M. Ebner, A. Eldiven, V. Wood, and H. A. Gasteiger, “Tortuosity of battery electrodes: validation of impedance-derived values and critical comparison with 3D tomography.” *J. Electrochem. Soc.*, **165**, A469 (2018).

22. J. Landesfeind, J. Hattendorff, A. Ehrl, W. A. Wall, and H. A. Gasteiger, "Tortuosity determination of battery electrodes and separators by impedance spectroscopy." *J. Electrochem. Soc.*, **163**, A1373 (2016).
23. M. Yamamoto, M. Takahashi, Y. Terauchi, A. Sakuda, Y. Kobayashi, S. Ikeda, and A. Sakuda, "Fabrication of composite positive electrode sheet with high active material content and effect of fabrication pressure for all-solid-state battery." *J. Ceram. Soc. Jpn.*, **125**, 391 (2017).
24. K. G. Naik, B. S. Vishnugopi, and P. P. Mukherjee, "Kinetics or transport: whither goes the solid-state battery cathode?" *ACS Appl. Mater. Interfaces*, **14**, 29754 (2022).
25. T. Asano, S. Yubuchi, A. Sakuda, A. Hayashi, and M. Tatsumisago, "Electronic and ionic conductivities of LiNi<sub>1/3</sub>Mn<sub>1/3</sub>Co<sub>1/3</sub>O<sub>2</sub>-Li<sub>3</sub>PS<sub>4</sub> positive composite electrodes for all-solid-state lithium batteries." *J. Electrochem. Soc.*, **164**, A3960 (2017).
26. S. Randau et al., "On the additive microstructure in composite cathodes and alumina-coated carbon microwires for improved all-solid-state batteries." *Chem. Mater.*, **33**, 1380 (2021).
27. N. Kaiser, S. Spannenberger, M. Schmitt, M. Cronau, Y. Kato, and B. Roling, "Ion transport limitations in all-solid-state lithium battery electrodes containing a sulfide-based electrolyte." *J. Power Sources*, **396**, 175 (2018).
28. Z. Siroma, T. Sato, T. Takeuchi, R. Nagai, A. Ota, and T. Ioroi, "AC impedance analysis of ionic and electronic conductivities in electrode mixture layers for an all-solid-state lithium-ion battery." *J. Power Sources*, **316**, 215 (2016).
29. T. A. Hendriks, M. A. Lange, E. M. Kiens, C. Baeumer, and W. G. Zeier, "Balancing partial ionic and electronic transport for optimized cathode utilization of high-voltage LiMn<sub>2</sub>O<sub>4</sub>/Li<sub>3</sub>InCl<sub>6</sub> solid-state batteries." *Batter. Supercaps*, **6**, e202200544 (2023).
30. D. Shin, J. S. Nam, C. T. Linh Nguyen, Y. Jo, K. Lee, S. M. Hwang, and Y.-J. Kim, "Design of densified nickel-rich layered composite cathode via the dry-film process for sulfide-based solid-state batteries." *J. Mater. Chem. A*, **10**, 23222 (2022).
31. M. So, G. Inoue, R. Hirate, K. Nunoshita, S. Ishikawa, and Y. Tsuge, "Effect of mold pressure on compaction and ion conductivity of all-solid-state batteries revealed by the discrete element method." *J. Power Sources*, **508**, 230344 (2021).
32. M. Yamamoto, Y. Terauchi, A. Sakuda, A. Kato, and M. Takahashi, "Effects of volume variations under different compressive pressures on the performance and microstructure of all-solid-state batteries." *J. Power Sources*, **473**, 228595 (2020).
33. M. B. Dixit, A. Parejiya, N. Muralidharan, R. Essehli, R. Amin, and I. Belharouak, "Understanding implications of cathode architecture on energy density of solid-state batteries." *Energy Storage Mater.*, **40**, 239 (2021).
34. T. Shi, Q. Tu, Y. Tian, Y. Xiao, L. J. Miara, O. Kononova, and G. Ceder, "High active material loading in all-solid-state battery electrode via particle size optimization." *Adv. Energy Mater.*, **2**, 1902881 (2019).
35. J. Park, K. T. Kim, D. Y. Oh, D. Jin, D. Kim, Y. S. Jung, and Y. M. Lee, "Digital twin-driven all-solid-state battery: unraveling the physical and electrochemical behaviors." *Adv. Energy Mater.*, **10**, 2001563 (2020).
36. F. Strauss, T. Bartsch, L. de Biasi, A.-Y. Kim, J. Janek, P. Hartmann, and T. Brezesinski, "Impact of cathode material particle size on the capacity of bulk-type all-solid-state batteries." *ACS Energy Lett.*, **3**, 992 (2018).
37. C. Park, S. Lee, K. Kim, M. Kim, S. Choi, and D. Shin, "Electrochemical properties of composite cathode using bimodal sized electrolyte for all-solid-state batteries." *J. Electrochem. Soc.*, **166**, A5318 (2019).
38. Y. Yamada, K. Watanabe, H. Kim, K. Suzuki, S. Hori, R. Kanno, and M. Hirayama, "Microstructure control of LiCoO<sub>2</sub>-Li<sub>10</sub>GeP<sub>2</sub>S<sub>12</sub> composite cathodes by adjusting the particle size distribution for the enhancement of all-solid-state batteries." *Batter. Supercaps*, **6**, e202300261 (2023).
39. C. König, V. Miß, L. Janin, and B. Roling, "Mitigating the ion transport tortuosity in composite cathodes of all-solid-state batteries by wet milling of the solid electrolyte particles." *ACS Appl. Energy Mater.*, **6**, acsaem.3c01242 (2023).
40. J. Kim, M. Eom, S. Noh, and D. Shin, "Effect of mixing method on the properties of composite cathodes for all-solid-state lithium batteries using Li<sub>2</sub>S-P<sub>2</sub>S<sub>5</sub> solid electrolytes." *J. Power Sources*, **244**, 476 (2013).
41. S. Noh, W. T. Nichols, M. Cho, and D. Shin, "Importance of mixing protocol for enhanced performance of composite cathodes in all-solid-state batteries using sulfide solid electrolyte." *J. Electroceramics*, **40**, 293 (2018).
42. H. Nakamura, T. Kawaguchi, T. Masuyama, A. Sakuda, T. Saito, K. Kuratani, S. Ohsaki, and S. Watano, "Dry coating of active material particles with sulfide solid electrolytes for an all-solid-state lithium battery." *J. Power Sources*, **448**, 227579 (2020).
43. V. Laue, N. Wolff, F. Röder, and U. Krewer, "Modeling the influence of mixing strategies on microstructural properties of all-solid-state electrodes." *Energy Technol.*, **8**, 1801049 (2020).
44. M. Cronau, M. Duchardt, M. Szabo, and B. Roling, "Ionic conductivity versus particle size of ball-milled sulfide-based solid electrolytes: strategy towards optimized composite cathode performance in all-solid-state batteries." *Batter. Supercaps*, **5** (2022).
45. A. Neumann, S. Randau, K. Becker-Steinberger, T. Danner, S. Hein, Z. Ning, J. Marrow, F. H. Richter, J. Janek, and A. Latz, "Analysis of interfacial effects in all-solid-state batteries with thiophosphate solid electrolytes." *ACS Appl. Mater. Interfaces*, **12**, 9277 (2020).
46. M. Kodama, A. Ohashi, H. Adachi, T. Miyuki, A. Takeuchi, M. Yasutake, K. Uesugi, T. Kaburagi, and S. Hirai, "Three-dimensional structural measurement and material identification of an all-solid-state lithium-ion battery by X-ray nanotomography and deep learning." *J. Power Sources Adv.*, **8**, 100048 (2021).
47. M. Kroll, M. Duchardt, S. L. Karstens, S. Schlabach, F. Lange, J. Hochstrasser, B. Roling, and U. Tallarek, "Sheet-type all-solid-state batteries with sulfide electrolytes: analysis of kinetic limitations based on a cathode morphology study." *J. Power Sources*, **505**, 230064 (2021).
48. S. Iwamoto, M. Kodama, K. Yanagi, Y. Haniu, Y. Fujii, N. Masuda, H. Higuchi, Y. Suetsugu, and S. Hirai, "Numerical simulations of all-solid-state batteries using specific contact area diameters for active materials determined by X-ray computed tomography." *J. Power Sources Adv.*, **21**, 100120 (2023).
49. M. Kodama, N. Horikawa, A. Ohashi, and S. Hirai, "Coupled nonlinear stress and electric field numerical simulation for all-solid-state lithium-ion batteries." *J. Power Sources Adv.*, **8**, 100049 (2021).
50. A. Ohashi, M. Kodama, N. Horikawa, and S. Hirai, "Effect of Young's modulus of active materials on ion transport through solid electrolyte in all-solid-state lithium-ion battery." *J. Power Sources*, **483**, 229212 (2021).
51. T. Shi, Y.-Q. Zhang, Q. Tu, Y. Wang, M. C. Scott, and G. Ceder, "Characterization of mechanical degradation in an all-solid-state battery cathode." *J. Mater. Chem. A*, **8**, 17399 (2020).
52. X. Gao et al., "Solid-state lithium battery cathodes operating at low pressures." *Joule*, **6**, 636 (2022).
53. D. Hlushkou, A. E. Reising, N. Kaiser, S. Spannenberger, S. Schlabach, Y. Kato, B. Roling, and U. Tallarek, "The influence of void space on ion transport in a composite cathode for all-solid-state batteries." *J. Power Sources*, **396**, 363 (2018).
54. W. Zhang et al., "Interfacial processes and influence of composite cathode microstructure controlling the performance of all-solid-state lithium batteries." *ACS Appl. Mater. Interfaces*, **9**, 17835 (2017).
55. A. L. Santhosha, L. Medenbach, J. R. Buchheim, and P. Adelhelm, "The indium-lithium electrode in solid-state lithium-ion batteries: phase formation, redox potentials, and interface stability." *Batter. Supercaps*, **414**, 359 (2019).
56. S. Bhattiprolu, 158b\_transfer\_learning\_using\_CNN\_weights\_VGG16\_RF. [https://github.com/bnsreenu/python\\_for\\_microscopists/blob/master/158b\\_transfer\\_learning\\_using\\_CNN\\_weights\\_VGG16\\_RF.py](https://github.com/bnsreenu/python_for_microscopists/blob/master/158b_transfer_learning_using_CNN_weights_VGG16_RF.py).
57. P. K. Charles, (2015), <https://keras.io>.
58. F. Pedregosa et al., "Scikit-learn: machine learning in python." *J. Mach. Learn. Res.*, **12**, 2825 (2011).
59. M. Ender, J. Joos, T. Carraro, and E. Ivers-Tiffée, "Quantitative characterization of LiFePO<sub>4</sub> cathodes reconstructed by FIB/SEM tomography." *J. Electrochem. Soc.*, **159**, A972 (2012).
60. J. Gostick, Z. Khan, T. Tranter, M. Kok, M. Agnaou, M. Sadeghi, and R. Jervis, "PoreSpy: a python toolkit for quantitative analysis of porous media images." *J. Open Source Softw.*, **4**, 1296 (2019).
61. S. Zhang and K. O. Findley, "Application of chords for quantitative characterization of multi-constituent microstructures." *Metallogr. Microstruct. Anal.*, **1**, 28 (2012).
62. T. G. Tranter, M. D.-R. Kok, M. Lam, and J. T. Gostick, "Pytrax: a simple and efficient random walk implementation for calculating the directional tortuosity of images." *SoftwareX*, **10**, 100277 (2019).
63. Math2Market GmbH, *GeoDict Simulation Software Release*, **2023** (2023).
64. S. Ohno, C. Rosenbach, G. F. Dewald, J. Janek, and W. G. Zeier, "Linking solid electrolyte degradation to charge carrier transport in the thiophosphate-based composite cathode toward solid-state lithium-sulfur batteries." *Adv. Funct. Mater.*, **31**, 2010620 (2021).
65. J. Y. Kim, J. Kim, S. H. Kang, D. O. Shin, M. J. Lee, J. Oh, Y. Lee, and K. M. Kim, "Efficient cell design and fabrication of concentration-gradient composite electrodes for high-power and high-energy-density all-solid-state batteries." *ETRI J.*, **42**, 129 (2020).
66. Z. Siroma, N. Fujiwara, S. Yamazaki, M. Asahi, T. Nagai, and T. Ioroi, "Mathematical solutions of comprehensive variations of a transmission-line model of the theoretical impedance of porous electrodes." *Electrochim. Acta*, **160**, 313 (2015).
67. M. Kodama, A. Takeuchi, M. Uesugi, T. Miyuki, H. Yasuda, and S. Hirai, "Nanoscale pore measurements in an all-solid-state lithium-ion battery with ultra-small-angle X-ray scattering (USAXS)." *J. Power Sources Adv.*, **12**, 100076 (2021).
68. A. Bielefeld, D. A. Weber, R. Rueß, V. Glavas, and J. Janek, "Influence of lithium ion kinetics, particle morphology and voids on the electrochemical performance of composite cathodes for all-solid-state batteries." *J. Electrochem. Soc.*, **169**, 020539 (2022).
69. E. J. Cheng, K. Hong, N. J. Taylor, H. Choe, J. Wolfenstine, and J. Sakamoto, "Mechanical and physical properties of LiNi<sub>0.33</sub>Mn<sub>0.33</sub>Co<sub>0.33</sub>O<sub>2</sub> (NMC)." *J. Eur. Ceram. Soc.*, **37**, 3213 (2017).
70. A. Sakuda, A. Hayashi, and M. Tatsumisago, "Sulfide solid electrolyte with favorable mechanical property for all-solid-state lithium battery." *Sci Rep.*, **3**, 2261 (2013).
71. A. Kato, M. Yamamoto, A. Sakuda, A. Hayashi, and M. Tatsumisago, "Mechanical properties of Li<sub>2</sub>S-P<sub>2</sub>S<sub>5</sub> glasses with lithium halides and application in all-solid-state batteries." *ACS Appl. Energy Mater.*, **1**, 1002 (2018).
72. E. Schlautmann et al., "Impact of the solid electrolyte particle size distribution in sulfide-based solid-state battery composites." *Adv. Energy Mater.*, 2302309 (2023).
73. J. Lee, S. Byun, H. Lee, Y. Roh, D. Jin, J. Lim, J. Song, C. B. Dzakpasu, J. Park, and Y. M. Lee, "Digital-twin-driven structural and electrochemical analysis of Li<sup>+</sup> single-ion conducting polymer electrolyte for all-solid-state batteries." *Battery Energy*, **2**, 20220061 (2023).
74. J. Park et al., "Unraveling the limitations of solid oxide electrolytes for all-solid-state electrodes through 3D digital twin structural analysis." *Nano Energy*, **79**, 105456 (2021).
75. M. Rana, Y. Rudel, P. Heuer, E. Schlautmann, C. Rosenbach, M. Y. Ali, H. Wiggers, A. Bielefeld, and W. G. Zeier, "Toward achieving high areal capacity in silicon-based solid-state battery anodes: what influences the rate-performance?" *ACS Energy Lett.*, **8**, 3196 (2023).

76. T.-T. Nguyen, A. Demortière, B. Fleutot, B. Delobel, C. Delacourt, and S. J. Cooper, "The electrode tortuosity factor: why the conventional tortuosity factor is not well suited for quantifying transport in porous li-ion battery electrodes and what to use instead." *NPJ Comput. Mater.*, **6**, 123 (2020), 10.1038/s41524-020-00386-4.
77. M. Clausnitzer, R. Mücke, F. Al-Jaljouli, S. Hein, M. Finsterbusch, T. Danner, D. Fattakhova-Rohlfing, O. Guillon, and A. Latz, "Optimizing the composite cathode microstructure in all-solid-state batteries by structure-resolved simulations." *Batter. Supercaps*, e202300167 (2023).
78. R. Koerver, I. Aygün, T. Leichtweiß, C. Dietrich, W. Zhang, J. O. Binder, P. Hartmann, W. G. Zeier, and J. Janek, "Capacity fade in solid-state batteries: interphase formation and chemomechanical processes in nickel-rich layered oxide cathodes and lithium thiophosphate solid electrolytes." *Chem. Mater.*, **29**, 5574 (2017).
79. R. Koerver, W. Zhang, L. de Biasi, S. Schweidler, A. O. Kondrakov, S. Kolling, T. Brezesinski, P. Hartmann, W. G. Zeier, and J. Janek, "Chemo-mechanical expansion of lithium electrode materials—on the route to mechanically optimized all-solid-state batteries." *Energy Environ. Sci.*, **11**, 2142 (2018).
80. G. Conforto, R. Ruess, D. Schröder, E. Trevisanello, R. Fantin, F. H. Richter, and J. Janek, "Editors' choice—quantification of the impact of chemo-mechanical degradation on the performance and cycling stability of NCM-based cathodes in solid-state li-ion batteries." *J. Electrochem. Soc.*, **168**, 070546 (2021).
81. F. Walther, R. Koerver, T. Fuchs, S. Ohno, J. Sann, M. Rohnke, W. G. Zeier, and J. Janek, "Visualization of the interfacial decomposition of composite cathodes in argyrodite-based all-solid-state batteries using time-of-flight secondary-ion mass spectrometry." *Chem. Mater.*, **31**, 3745 (2019).
82. J. Ruhl, L. M. Riegger, M. Ghidui, and W. G. Zeier, "Impact of solvent treatment of the superionic argyrodite  $\text{Li}_6\text{PS}_5\text{Cl}$  on solid-state battery performance." *Adv. Energy Sustain. Res.*, **2**, 2000077 (2021).
83. A.-K. Hatz, R. Calaminus, J. Fejoo, F. Treber, J. Blahusch, T. Lenz, M. Reichel, K. Karaghiosoff, N. M. Vargas-Barbosa, and B. V. Lotsch, "Chemical stability and ionic conductivity of LGPS-type solid electrolyte tetra- $\text{Li}_7\text{SiPS}_8$  after solvent treatment." *ACS Appl. Energy Mater.*, **4**, 9932–9943 (2021).
84. W. Zhang, T. Leichtweiss, S. Culver, R. Koerver, D. Das, D. A. Weber, W. G. Zeier, and J. Janek, "The detrimental effects of carbon additives in solid-state batteries using  $\text{Li}_{10}\text{GeP}_2\text{S}_{12}$  as solid electrolyte." *ACS Appl. Mater. Interf.*, **9**, 35888 (2017).